

Understanding Mercury's Thermochemical Evolution Using a Geochemical and Geophysical  
Lens

Priyanka Bose

Thesis submitted to the faculty of the Virginia Polytechnic Institute and State University in  
partial fulfillment of the requirements for the degree of

Master of Science

In

Geosciences

Dr. Megan S. Duncan, Co-Chair

Dr. Scott D. King, Co-Chair

Dr. James A. Spotila, Member

Dr. Ryan M. Pollyea, Member

Dr. Mark J. Caddick, Member

May 3<sup>rd</sup>, 2024

Blacksburg, Virginia

Keywords: Mercury, Thermochemical Evolution, Mantle Melt Parameterization, Inner Core  
Formation, Top-Down Core Crystallization, Bottom-Up Core Crystallization

# Understanding Mercury's Thermochemical Evolution Using a Geochemical and Geophysical Lens

Priyanka Bose

## ABSTRACT

Mercury is currently the most enigmatic planet within the inner Solar System; however, data from MESSENGER has started to illuminate the history of Mercury's interior. Geophysical and geochemical data from MESSENGER suggest Mercury consists of a thin silicate bearing layer (including the regolith, crust, and mantle) with cooled surface lavas derived from a highly reduced mantle, and a large Fe rich core with some amount of light element and a possible solid inner core. To understand how Mercury evolved under these non-Earth-like conditions, a modified thermochemical evolution model was created to account for variable core densities, different core crystallization methods, and a more reduced mantle composition. This model was used to provide insights into the initial conditions that Mercury possibly experienced after formation. While the model has limitations, the model results suggest Mercury's interior most likely began cooling from an initial mantle temperature of 1600 K, had a relatively high mantle reference viscosity of  $10^{21}$ – $10^{22}$  Pa s, with core sulfur contents between 0.05–8.9 wt.% S, based on present day constraints derived from MESSENGER data. More data from BepiColombo will provide additional insights into the inner workings of Mercury, leading to more information about the initial conditions of the inner solar system, and non-Earth like evolution conditions.

# Understanding Mercury's Thermochemical Evolution Using a Geochemical and Geophysical Lens

Priyanka Bose

## GENERAL AUDIENCE ABSTRACT

Mercury is the most mysterious planet in the inner Solar System, suggested by observations from the MESSENGER mission. These observations shine a light on potential processes occurring within Mercury as it evolved over time. Scientific instruments aboard MESSENGER indicate that Mercury has a very thin surface layer of broken rocks, a thin crustal layer covered by lavas erupted from a melt formed in a relatively thin, FeO poor mantle, and a large metal rich core made from Fe and some quantity of a light element. These conditions are different than those seen on Earth: a thick crust covered by a layer of varied thickness made up of loose unconsolidated rocks and dust, a large mantle with more FeO, and a smaller core to planet ratio. To understand how these non-Earth like conditions affect how the planet's interior changes with time, a modified evolution model was created to track the changes in heat and chemistry within Mercury. This model accounts for complications like a dynamic core density that changes with a growing inner core, the formation method of the inner core, and the FeO poor mantle composition. Using this model offers illumination on the conditions Mercury experienced after it formed. This model is limited, but results suggest that Mercury's mantle began at an initial mantle temperature of 1600 K, and a mantle reference viscosity of  $10^{21}$ – $10^{22}$  Pa s, indicating the mantle was less likely to flow easily. Model results also suggest the core contained some sulfur from 0.05–8.9 wt.% S, derived from the MESSENGER data. BepiColombo, a new Mercury mission, will provide some perspectives on the interior of Mercury, leading to more detailed information about conditions present after planetary formation and the effect of non-Earth like conditions on a planet's interior as it cools.

## ACKNOWLEDGEMENTS

I am grateful for all the support from my advisors: Dr. Scott King and Dr. Megan Duncan, including their willingness to advise me after my first advisor Dr. Bob Lowell passed away, and their advice on this project. This thesis would not have been possible without the support of my thesis committee: Dr. Ryan Pollyea, Dr. James Spotila, and Dr. Mark Caddick. I am extremely thankful to April Newcomer, Sharon Collins, and Mary-Jane Smith for their helpful advice, support, and encouragement in bringing this to fruition. I would also like to extend my deepest gratitude to my partner, Nathan Raeker-Jordan, for his unwavering support and confidence in me. I am extremely grateful to my parents: Shatarupa and Partha, and to the rest of my family for their continuous belief, encouragement, and support in me. Special thanks go to Nathan and Jonny for their help with Python coding. I cannot express enough thanks to my friends who have always supported me while at Virginia Tech: Allie, Aly, Alix, Alaina, Jonny, Ella, Rose, Tarisa, Natalia, Ezster, Gina, Kass, Kelsey, Chanté, Kelsey, and Rachel. I am extremely appreciative of the mentorship I have received from Dr. Parvathy Prem, Dr. Kim Lau, Dr. Emily Martin, Dr. Tushar Mittal, Dr. Julia Carr, Erica Howat, and Dr. Claire Cleveland. Finally, I would like to thank VT MAOP for their financial support.

# Table of Contents

1. Introduction to Project	1
2. A Holistic Geochemical and Geophysical Model of the Thermochemical Evolution of Mercury	3
2.1. Introduction	3
2.1.1. MESSENGER Results	3
2.1.2. Northern Smooth Plains	4
2.1.3. Core Composition	5
2.1.4. Prior Thermochemical Evolution Models	6
2.2. Thermochemical Evolution Model Description	9
2.2.1. Model Setup	9
2.2.2. The Core	13
2.2.3. The Mantle	18
2.2.4. The Crust	22
2.2.5. Planetary Contraction	23
2.3. Results	24
2.3.1. Changing Core Density and Melting	24
2.3.2. The Fe-Free Melt Parameterization	26
2.3.3. Varying all three input parameters in a grid	27
2.4. Discussion	32
2.4.1. Comparing the peridotite and Fe-free mantle melt parametrizations	32
2.4.2. Comparing the model results with present day Mercury	33
2.4.3. Inner core calculations	35
2.4.4. Model Limitations and future work suggestions	36
2.5. Conclusions	38
3. Conclusions of Project	40
4. References	41
A. Modified NORMS Calculation	49
B. Core Parameters	51
B.1. The calculation of the inner and outer core density values	51
B.2. The Fe+S Melting Curve	53
C. Mantle Parameters	55
C.1. Volumetric heat flux from radiogenic heating within the mantle	55
C.1.1. Calculating the temperatures at the base of the stagnant lid and the bottom of the convecting mantle	56
C.1.2. Calculating $\epsilon_m$ for the mantle	57
C.1.3. Calculating the thermal profile of the silicate part of Mercury	57
C.1.4. Calculating the thermal boundary layer thicknesses in the mantle	58

C.1.5. Mantle convection velocity	59
D. Supplementary Data Visualizations: Relationships with Mantle Reference Viscosity and Initial Mantle Temperature	60
E. Moment of Inertia Calculation	65
E.1. Calculating planetary mass	65
E.2. Calculating moment of inertia factor	65

## List of Figures

**Figure 1-1:** A false colored image of Mercury taken by MESSENGER. The younger surface material is colored as light blue or white, the darker blue areas are the low-reflectance material regions, and the tan areas indicate regions of lava plains on Mercury’s surface. The figure was taken from NASA’s Science on a Sphere catalog (National Oceanic and Atmospheric Administration, 2013)..... 2

**Figure 2-1:** Model schematics (**left**) A cross-section of Mercury’s interior showing the crust, the mantle, and the core partitions, along with the approximate thicknesses of each main layer (*Margot et al.*, 2018). The solid lines represent interfaces between the different partitions of Mercury, while the dashed lines represent the growing thermal boundary layers (TBLs) in the mantle. A representative solid inner core is shown as well. (**right**) A thermal profile through Mercury. The temperature reaches its highest point within the inner core at the inner core liquidus, then decreases throughout the core gradually until it reaches the core-mantle boundary (CMB), where the temperature slightly decreases as it crosses the bottom TBL ( $\delta_b$ ), and then decreases adiabatically from the bottom TBL to the top TBL ( $\delta_t$ ). After the temperature progresses through the top TBL, it rapidly decreases until it reaches the surface. After Figure 1 from *Stevenson et al.* (1983). .... 10

**Figure 2-2:** The method used to calculate inner core crystallization. Based on the updated melting curve from *Rivoldini et al.* (2011), both top-down and bottom-up core crystallization processes are possible for Mercury. The green lines indicate the steps to calculate the inner core crystallization using the top-down core crystallization approach, and the orange lines denote the steps to calculate the inner core crystallization using the bottom-up core crystallization approach. Steps that are used in both approaches are shown in black, and the pathways are described in the text. .... 17

**Figure 2-3:** Model results using a peridotite melt parameterization (*Takahashi*, 1990) and the same inputs as *Grott et al.* (2011) as a function of time. (**a**) Thermal profile of the core (orange dotted line) and the mantle (blue dash dot line). (**b**) Calculated heat fluxes: the core heat flux ( $q_c$  – dotted orange line), the mantle heat flux ( $q_m$  – blue dash dot line), and the surface heat flux ( $q_s$  – solid green line). (**c**) The silicate radial profile: the crustal depth ( $D_{cr}$  – solid red line), the stagnant lid depth ( $D_{sl}$  – dotted purple line), and the melt zone in the mantle ( $D_{mz}$  – black dash dot line). (**d**) Contraction profiles: radial contraction due to inner core formation ( $R_{ic}$  – orange dotted line), due to mantle differentiation ( $R_{md}$  – blue dot dash line), due to secular cooling ( $R_{sec}$  – black dash-dot line), and total planet radial contraction ( $R_{tot}$  – solid black line). (**e**) Calculated volume averaged mantle melt fraction. (**f**) Calculated inner core radius. .... 25

**Figure 2-4:** Model results using a Fe-free melt parameterization (*Namur et al.*, 2016) and the same inputs as *Grott et al.* (2011) as a function of time. These results are overlaid on top of the peridotite melt parameterization (Figure 2-3; faded results) to highlight the difference in the model results. (**a**) Thermal profile of the core (orange dotted line) and the mantle (blue dash dot line). (**b**) Calculated heat fluxes: the core heat flux ( $q_c$  – dotted orange line), the mantle heat flux ( $q_m$  – blue dash dot line), and the surface heat flux ( $q_s$  – solid green line). (**c**) The silicate radial profile: the crustal depth ( $D_{cr}$  – solid red line), the stagnant lid depth ( $D_{slr}$  – dotted purple line), and the melt zone in the mantle ( $D_{mz}$  – black dash dot line). (**d**) Radial contraction profiles: due to inner core formation ( $R_{ic}$  – orange dotted line), due to mantle differentiation ( $R_{md}$  – blue dot dash line), due to secular cooling ( $R_{sec}$  – black dash-dot line), and total radial contraction of the planet ( $R_{tot}$  – solid black line). (**e**) Calculated volume averaged mantle melt fraction. (**f**) Calculated inner core radius. .... 26

**Figure 2-5:** Calculated present day crustal thickness. The initial mantle temperature increases left to right from 1600 K to 1900 K, symbols correspond to different viscosity values: blue circles –  $10^{19}$  Pa s, orange squares –  $10^{20}$  Pa s, green diamonds –  $10^{21}$  Pa s, red stars –  $10^{22}$  Pa s. The red and gray bands indicate the bounds of crustal thickness estimates for present day Mercury: 15–53 km (*Padovan et al.*, 2015; *Sori*, 2018). Model results within the band are indicative of possible initial conditions for Mercury. .... 27

**Figure 2-6:** Calculated time of mantle melt cessation. The initial mantle temperature increases left to right from 1600 K to 1900 K, symbols correspond to different viscosity values as in Figure 2-5. The gray band represents the timing constraint of cessation of effusive volcanism by 3.7–3.5 Ga (*Byrne et al.*, 2016). Model results that plot at or above the band are relevant for present day Mercury. .... 28

**Figure 2-7:** Calculated present day inner core radii. The initial mantle temperature increases left to right from 1600 K to 1900 K, symbols correspond to different viscosity values as in Figure 2-5. The gray band indicates the upper limits on the present day inner core of radius:  $1325 \pm 250$  km (*Breuer et al.*, 2015; *Dumberry and Rivoldini*, 2015). Model values that plot within or under the band indicate possible conditions experienced by Mercury. .... 29

**Figure 2-8:** Present day total radial contraction. The initial mantle temperature increases left to right from 1600 K to 1900 K, symbols correspond to viscosity values as in Figure 2-5. The gray band represents the bounds on the total radial contraction estimates of 2–7 km (*Byrne et al.*, 2014; *Claeys and Morbidelli*, 2015; *Watters*, 2021). Model results plotting within that band are relevant for present day Mercury. .... 29

**Figure 2-9:** The calculated present day Mercury mass values. The mantle viscosity values increase from left to right from  $10^{19}$  Pa s to  $10^{22}$  Pa s, and initial mantle temperature decreases from top to bottom from 1900 K to 1600 K. The black line indicates the mass of Mercury at  $3.3 \times 10^{23}$  kg (*Margot et al.*, 2018). Successful models plot on the black line. .... 30

**Figure 2-10:** The calculated present day Mercury polar MOI factor. The mantle viscosity values increase from left to right from  $10^{19}$  Pa s to  $10^{22}$  Pa s, and initial mantle temperature decreases from top to bottom from 1900 K to 1600 K. The gray band indicates the range of Mercury’s MOI factor  $0.346 \pm 0.009$  (*Margot et al.*, 2012). Model values plotting within the band match Mercury. .... 31

**Figure A-1:** (A) The major mineral breakdown of the non-sulfide bearing minerals of the NSP-HMg region. The main mineral components for this region were plagioclase, followed by orthopyroxene, olivine, clinopyroxene, orthoclase, and other minor minerals, described above. (B) The sulfide breakdown of the NSP-HMg region of the surface is shown here, which was found to be predominantly iron sulfide, then titanium sulfide, and chromium sulfide. .... 50

**Figure B-1:** (a) The solid and liquid Fe density relationship with the pressure of the core. The dark blue line shows the trend in the solid Fe density, while the brown line shows the trend in the liquid Fe density. The black dashed and dash-dot line indicate the pressure boundary of the CMB, and the central pressure of the planet, respectively. The black line indicates the constant core density used in the model created by *Grott et al.* (2011). (b) The liquid FeS density as a function of core S content. .... 52

**Figure D-1:** Model result for varied mantle reference viscosity. (First row) The present day crustal thickness. The gray band indicates the bounds of the present day crustal thickness estimate:

15–53 km (*Padovan et al.*, 2015; *Sori*, 2018), and models that have points plotted in the band represent models that have crustal thickness values which fit within the crust constraint. **(Second row)** The present day inner core radius. The gray band indicates the upper bound of the present day inner core estimate:  $1325 \pm 250$  km (*Breuer et al.*, 2015; *Dumberry and Rivoldini*, 2015), and models that have points plotted in or below the gray band represent models with appropriately sized present day inner core radii. **(Third row)** The timing of melt cessation. The gray band indicates the upper extent of melt generation (effusive volcanism) cessation by 3.7–3.5 Ga (*Byrne et al.*, 2016), and models that have points plotted in or below the gray band represent models with appropriate ending times for partial melt generation (effusive volcanism). **(Fourth row)** The present day total radial contraction. The gray band shows the bounds of the present day total radial contraction estimates: 2–7 km (*Byrne et al.*, 2014; *Claeys and Morbidelli*, 2015; *Watters*, 2021), and models with points plotted within the gray band represent models with appropriate total planet radial contraction values. **(Fifth row)** The present day Mercury mass. The black line shows the bounds of the present day Mercury mass and models with points plotted on the black line represent models with a present day mass that falls within the constraints. **(Sixth row)** The present day calculated Mercury polar MOI factor. The gray band shows the bounds of the present day Mercury polar MOI estimates, and models with points plotted within the gray band represent models with appropriate Mercury polar MOI factors..... 61

**Figure D-2:** Model result for varied initial mantle temperature. **(First row)** The present day crustal thickness. The gray band indicates the bounds of the present day crustal thickness estimate: 15–53 km (*Padovan et al.*, 2015; *Sori*, 2018), and models that have points plotted in the band represent models that have crustal thickness values which fit within the crust constraint. **(Second row)** The present day inner core radius. The gray band indicates the upper bound of the present day inner core estimate:  $1325 \pm 250$  km (*Breuer et al.*, 2015; *Dumberry and Rivoldini*, 2015), and models that have points plotted in or below the gray band represent models with appropriately sized present day inner core radii. **(Third row)** The timing of melt cessation. The gray band indicates the upper extent of melt generation (effusive volcanism) cessation by 3.7–3.5 Ga (*Byrne et al.*, 2016), and models that have points plotted in or below the gray band represent models with appropriate ending times for partial melt generation (effusive volcanism). **(Fourth row)** The present day total radial contraction. The gray band shows the bounds of the present day total radial contraction estimates: 2–7 km (*Byrne et al.*, 2014; *Claeys and Morbidelli*, 2015; *Watters*, 2021), and models with points plotted within the gray band represent models with appropriate total planet radial contraction values. **(Fifth row)** The present day Mercury mass. The black line shows the bounds of the present day Mercury mass and models with points plotted on the black line represent models with a present day mass that falls within the constraints. **(Sixth row)** The present day calculated Mercury polar MOI factor. The gray band shows the bounds of the present day Mercury polar MOI estimates, and models with points plotted within the gray band represent models with appropriate Mercury polar MOI factors..... 63

## List of Tables

<b>Table 2-1:</b> Model Parameters .....	11
<b>Table 2-2:</b> Varied Parameters in the Model .....	13
<b>Table B-1:</b> Liquid Fe+S Alloy Reference Bulk Modulus and Density Components .....	51
<b>Table B-2:</b> Core Adiat and Melt Curve Parameters .....	54
<b>Table C-3:</b> Heat producing element parameters .....	56

# 1. Introduction to Project

Observations of Mercury, a small planet close to the Sun in the inner Solar System, were first recorded in the 14<sup>th</sup> century BCE (*Schaefer, 2007*). However, not much information has been determined about Mercury, due to its location next to the Sun, which causes difficulties in Earth-based ground observations of Mercury through a telescope; and an extreme temperature environment in the area surrounding Mercury's orbit making spacecraft observations difficult even with thermal shields (*ESA; Santo et al., 2001; Strom, 1979*). Sending a spacecraft to Mercury is also challenging and requires multiple gravity assists from other planets to adjust the spacecraft's trajectory (*Strom, 1979*). However, even with these difficulties, two spacecrafts have obtained data from Mercury from flybys and orbital insertions: Mariner 10 (1974–1975) and the MESSENGER (MErcury Surface Space ENvironment GEOchemistry and Ranging) mission from 2011–2015 (*Solomon et al., 2001*). BepiColombo is currently on its way to Mercury to obtain more information about Mercury's surface and interior. Major findings from the Mariner 10 mission include Mercury's mean uncompressed density, which indicated a large metal core and a thin silicate shell; surface reflectance data and images of 45% of the surface; Mercury mass estimates; the general composition of Mercury's exosphere; and the weak magnetic field (*Ness et al., 1975, 1976; Strom, 1979*). Almost 40 years later, MESSENGER confirmed many of the findings from the Mariner 10 mission and provided additional information about Mercury's surface composition and geology, density and gravity profiles, and the weak magnetosphere (*McCoy and Nittler, 2014*). With these combined datasets, it is possible to glean information about the smallest and most enigmatic rocky planet in the solar system. Multiple thermochemical evolution models, discussed in detail in the text, have attempted to determine the initial conditions Mercury experienced, and its evolution to its present day state using the findings from these missions.

The thermochemical evolution model used in this study updates prior evolution models with geochemical and geophysical constraints from the MESSENGER mission to evaluate potential initial conditions experienced by Mercury. Major model updates include a core algorithm that accounts for the core crystallizing from the top-down (like Ganymede) or bottom-up (like Earth) or a combination of both, and a more appropriate mantle melt parameterization. Results from this study will provide a geochemically relevant thermochemical evolution path for Mercury and will attempt to constrain the initial conditions Mercury experienced.

Mercury is classified as a geochemical endmember based on its surface compositions derived from the MESSENGER mission (*Vander Kaaden et al.*, 2017). Therefore, understanding how Mercury has evolved from its initial conditions can potentially illuminate the formation conditions of the inner planets and how heat is transferred in non-Earth-like settings. These findings will elucidate some of the evolutionary pathways available to the inner planets of the Solar System, providing insights into the evolution of rocky planets and even Mercury-like exoplanet evolution (*Mallama*, 2009). Exploring how Mercury evolved, furthers NASA's goal of understanding the history of planets (*National Academies of Sciences*, 2023). Thus, the thermochemical evolution of Mercury is important to understand the Solar System and space in general.



**Figure 1-1:** A false colored image of Mercury taken by MESSENGER. The younger surface material is colored as light blue or white, the darker blue areas are the low-reflectance material regions, and the tan areas indicate regions of lava plains on Mercury's surface. The figure was taken from NASA's Science on a Sphere catalog (National Oceanic and Atmospheric Administration, 2013)

## 2. A Holistic Geochemical and Geophysical Model of the Thermochemical Evolution of Mercury

### 2.1. Introduction

Mercury is the smallest terrestrial planet and has an enigmatic formation and evolution history, as evidenced by a high metal-silicate ratio (*Malavergne et al.*, 2014) and a unique surface composition (*Nittler et al.*, 2018). Because of these qualities, Mercury is classified as a Solar System endmember (*Vander Kaaden et al.*, 2017). Therefore, understanding how Mercury evolved will provide insights into how non-Earth-like conditions affect planetary evolution, and the materials from which the terrestrial planets formed.

#### 2.1.1. MESSENGER Results

The MESSENGER (MErcury Surface, Space, ENvironment, GEOchemistry, and Ranging) mission used both geochemical (X-Ray Spectrometer – XRS, Gamma-Ray Spectrometer – GRS, and Neutron Spectrometer – NS) and geophysical (Radio Science – RS and Mercury Laser Altimeter – MLA) instruments to collect data about Mercury’s surface and interior (*Solomon et al.*, 2001; *Solomon and Anderson*, 2018). The geophysical data was used to calculate gravity and density profiles and predicted a structure of Mercury’s interior (*McCoy and Nittler*, 2014; *Solomon et al.*, 2001; *Solomon and Anderson*, 2018). This structure is a three layer planet with a relatively thin crust compared to the total planetary radius (15–53 km; *Padovan et al.*, 2015; *Sori*, 2018), mantle (~300–400 km thick), and a large core (2040 km thick; *Margot et al.*, 2018). From the moment of inertia and bulk density derived from the MESSENGER mission data (*Margot et al.*, 2012), prior thermochemical evolution models used MESSENGER data to estimate the thicknesses of the mantle and core (*Dumberry and Rivoldini*, 2015; *Grott et al.*, 2011; *Hauck et al.*, 2013). The silicate part of Mercury is estimated to be  $420 \pm 30$  km thick (*Hauck et al.*, 2018), and the core is estimated to have a radius of 2000–2040 km (*Margot et al.*, 2018). There is a suggestion of an inner core (*Genova et al.*, 2019), however, the size of the inner core is not well constrained with current available data, and the maximum inner core radius is constrained to  $1325 \pm 250$  km (*Breuer et al.*, 2015; *Dumberry and Rivoldini*, 2015).

Mercury’s planetary radius ( $2439.2 \pm 0.5$  km) was determined from radio occultation measurements made during the MESSENGER flybys prior to its insertion into orbit (*Perry et al.*, 2011). The surface gravity was determined from RS measurements during MESSENGER’s orbit

(*Margot et al.*, 2018), and the surface temperature was determined to be 440 K based on black-body temperature calculations (Williams, Mercury Fact Sheet). From the density profiles derived from the RS and MLA data, the density estimates for the mantle and crust were obtained (*Beuthe et al.*, 2020; *Goossens et al.*, 2022; *Guerrero et al.*, 2021; *Hauck et al.*, 2013; *Margot et al.*, 2018; *Peterson et al.*, 2021; *Riner et al.*, 2008). MESSENGER also provided estimates of the radial thicknesses of the crust, mantle, and core via modeling that constrained by the RS data (*Margot et al.*, 2012). Updated polar moment of inertia (MOI) calculations based off these constraints are  $0.346 \pm 0.009$  (*Margot et al.*, 2012).

Geochemical measurements of Mercury's surface lavas showed enrichments in Mg and S, and deficiencies in Fe, when compared to mid-ocean ridge basalts on Earth (*Gale et al.*, 2013; *Nittler et al.*, 2018). Additionally, the high MgS and CaS concentrations observed at the surface (*Nittler et al.*, 2011), and the high metal-silicate ratio, led to predictions that Mercury formed under highly reduced conditions (*Namur et al.*, 2016). MESSENGER also measured Th and K on the surface of Mercury (*Nittler et al.*, 2018), which indicates that these radioactive elements are also in Mercury's mantle and in the crust. Further study of the geochemical data distinguished nine geochemical and morphological terranes: the high Mg region; the high Mg region with high Ca and S; the Northern Smooth/Volcanic Plains with high Mg content; the Northern Smooth/Volcanic Plains with low Mg content; the Rachmaninoff Basin; the pyroclastic deposit; the high Al region; the interior plains in the Caloris Basin; and the intermediate terrain (*Vander Kaaden et al.*, 2017). We focused on the youngest of these terranes: the Northern Smooth/Volcanic Plains (NSP; both Mg containing regions).

### *2.1.2. Northern Smooth Plains*

Located within the Borealis Planitia region of Mercury, the NSP are an ideal terrane to decipher Mercury's thermal and chemical evolution. Volcanism was the primary crust formation mechanism as the lava likely erupted into thin laminar sheets that cooled to form the crust (*Charlier and Namur*, 2019; *Head et al.*, 2011; *McCoy and Nittler*, 2014). From the surface composition, it is thought the magma did not experience any significant fractionation during its ascent from the mantle to surface (*McCoy and Nittler*, 2014; *Robinson and Taylor*, 2001). The NSP has an estimated lava flow volume of  $4-8 \times 10^6 \text{ km}^3$ , comparable to the Deccan and Siberian Traps on Earth (*Vander Kaaden et al.*, 2017). As Mercury's mantle is significantly thinner than Earth's mantle, the amount of melt formed from a considerably smaller area than the melt that formed the

Deccan and Siberian flood basalts. *Byrne et al.* (2016) determined the NSP was deposited ~3.5 Ga, and that effusive volcanism ended on Mercury between 3.7–3.5 Ga. Prior studies determined the surface composition and lithology of the region to be a trachyte/boninite (*McCoy et al.*, 2018). More recently, the surface NSP composition was reanalyzed through the MELTS and pMELTS software and high pressure-temperature experiments to determine the melting processes and mantle source of the mercurian mantle (*Namur et al.*, 2016). They parameterized an Fe-free solidus and liquidus based on a simplified composition (CMASN: Ca-Mg-Al-Si-Na), to account for the low Fe and high Na<sub>2</sub>O abundance, suggesting a Fe-free mantle composition based on MESSENGER data (*Namur et al.*, 2016). This geochemically relevant mantle solidus and liquidus has not been incorporated into many thermochemical evolution models, which is what this study does.

### 2.1.3. Core Composition

Data from the Mariner 10 mission indicated that Mercury had a weak magnetic field (*Ness et al.*, 1975, 1976; *Spohn*, 1991), which was confirmed by the MESSENGER mission (*Margot et al.*, 2018). The core is thought to contain some concentration of light elements (e.g., S, Si, C), because magnetic dynamo models of Mercury with either an Fe or Fe-Ni core composition indicate the core would be completely solidified at present day (*Solomon*, 1976). Thus, a light element is required to keep Mercury's core partially liquid. A common light element candidate for the core is sulfur (*Breuer et al.*, 2015; *Chabot et al.*, 2014; *Dumberry and Rivoldini*, 2015; *Grott et al.*, 2011; *Hauck et al.*, 2004; *Hauck et al.*, 2013; *Hauck et al.*, 2018; *Margot et al.*, 2018; *Michel et al.*, 2013; *Nittler et al.*, 2018), and the current core S concentration was constrained between 2.8–8.9 wt.% (*Knibbe and van Westrenen*, 2015). A compositional mixture of Fe, S, Si, and C is thought to be a more representative core composition (*Genova et al.*, 2019; *Hauck et al.*, 2013; *Knibbe and van Westrenen*, 2015; *Margot et al.*, 2018; *Vander Kaaden et al.*, 2020), but is out of the scope of this project due to the complexity of the partitioning between Fe, S, Si, and C. An Fe+S core composition is assumed for simplicity, as S can be assumed to completely partition into the liquid part of the core rather than the solid inner core. Additionally, this Fe+S core composition allows the model results to be compared to the results of prior models of Mercury's thermochemical evolution (*Grott et al.*, 2011; *Michel et al.*, 2013; *Tosi et al.*, 2013). Past models run with the Fe+S core composition have resulted in solutions agreeing with both Mercury's polar

moment of inertia and the fractional polar moment of inertia of the outer silicate shell (*Genova et al.*, 2019), and thus this choice is valid for a thermochemical evolution model of Mercury.

#### 2.1.4. Prior Thermochemical Evolution Models

While Mercury's thermochemical evolution was studied previously, most studies approximated melting with a peridotite solidus (*Grott et al.*, 2011; *Hauck et al.*, 2013; *Michel et al.*, 2013; *Tosi et al.*, 2013; *Tosi et al.*, 2015). A peridotite solidus is not appropriate for Mercury, due to the low FeO content of Mercury's mantle (*Malavergne et al.*, 2014). The Fe-free melting parameterization (*Namur et al.*, 2016) is more appropriate for Mercury's mantle, and will provide a better approximation for the mantle evolution. Incorporating this geochemically derived mantle melt parameterization into a thermochemical evolution model will give more reliable insights into Mercury's evolution. This study focuses on modifying a previous thermochemical evolution model for Mercury to understand how the planet's interior changed with a more realistic mantle solidus and core crystallization regime. Our model builds upon models from previous studies described below.

*Stevenson et al.* (1983) used a 1D thermal evolution model with parameterized mantle convection to model all the terrestrial planets in the Solar System with a simple Nusselt-Rayleigh number relation. They assumed that Mercury's dynamo was derived from thermal and chemical convection, radiogenic elements were only within the mantle, and Mercury's mantle was cooling from the solidus temperature, while the core was cooling from a subsolidus state. In their model, an inner core forms within the first 1 Myr of Mercury's formation, and grows to about 1750 km, with mantle convection persisting to present day. Additionally, they attempted to constrain the thickness of the outer core and suggested that Mercury's magnetic field was a thin-shelled dynamo. *Hauck et al.* (2004) modeled the thermochemical evolution of Mercury by building on the *Stevenson et al.* (1983) model, coupling their parameterized convection model to a partial melt model and incorporating conduction within the mantle. They suggest that the present day state of Mercury is achieved if the mantle is dominated by a rheology of dry olivine, the bulk core has 6.5–7.5 wt.% S, and the radiogenic heat production in the mantle is dominated by  $^{232}\text{Th}$ .

*Grott et al.* (2011) used a 1D parameterized thermochemical evolution model that accounted for the presence of an insulating megaregolith and volatiles within the interior of Mercury's structure. They investigated the timing of melt cessation within Mercury's mantle and calculated the global total radial contraction by determining the radial changes caused by the

secular cooling of Mercury, the inner core formation, and the radial expansion determined from the mantle differentiating into the crust.

*Hauck et al.* (2013) used the normalized polar moment of inertia (MOI) and fractional polar MOI of Mercury's solid outer shell to constrain their 1D parameterized thermochemical evolution models of Mercury, with an investigation of potential core compositions. This included cores composed of Fe-FeS, Fe-FeSi, and Fe-S-Si. With these added constraints, and their core composition variations, they determined the radius of Mercury's core and proposed the occurrence of an FeS rich layer at the top of the outer core.

*Michel et al.* (2013) used MESSENGER-derived constraints to model mantle convection and melt generation using Citcom. They found that mantle convection can persist within the mantle for extended periods of time, and the convecting mantle can generate substantial amounts of melt in these models.

*Rivoldini and Van Hoolst* (2013) used two models to determine Mercury's interior structure, which they constrained by the gravity field and rotation parameters calculated for Mercury from the MESSENGER mission. First, they used a 1D parameterized evolution model to examine the effect of five potential Mercury mantle compositions, a crust with a known thickness and density, and two mantle temperature profiles. In their second model, they used Bayesian inversion on their 1D parameterized evolution model to determine which set of inputs from a large array of mantle density profiles, crust thickness and density profiles, and the CMB temperature best fit the low-degree gravity field found on Mercury.

*Tosi et al.* (2013) ran multiple Monte Carlo simulations of their 1D parameterized thermochemical evolution models using revised constraints from the MESSENGER data and compared their results to both 2D and 3D thermochemical evolution models to gain a better understanding of how Mercury evolved. The results of their study suggest a typical evolution path for Mercury where the mantle initially gets heated leading to a large supply of partial melt in the mantle. Mercury's cooling is primarily driven by secular cooling that potentially occurs today, and that Mercury's mantle is no longer actively convecting, but is in a conducting state. *Tosi et al.* (2015) discussed the effect that a non-constant surface temperature has on the thermochemical evolution of Mercury calculated using GAIA (*Hüttig et al.*, 2013). Results from this study indicate that Mercury's shape was influenced by its elastic lithosphere which was estimated to be 110–180 km thick.

*Dumberry and Rivoldini* (2015) used a 1D 2-layer interior structure model of Mercury to investigate Mercury's inner core size and core-crystallization regime, with a core composition of Fe-FeS. They assumed ideal mixing between liquid Fe and liquid Fe+10 wt.% S for the core and used the 3<sup>rd</sup> order Birch-Murnaghan equation of state (EoS) to determine thermodynamic properties of the core. Their results were constrained by Mercury's moment of inertia and the amplitude of the libration of Mercury's silicate shell. Within their model, they investigated Mercury's core crystallization regime, but used an Fe-FeS melt curve that was appropriate for Earth's core conditions rather than Mercury's core conditions. Their results constrain the inner core to  $1325 \pm 250$  km and suggest that Mercury's inner core likely formed by the top-down Fe snow method.

*Knibbe and van Westrenen* (2015) contributed models of Mercury with potential core compositions of Fe-S or Fe-Si, and constrained their calculation of Mercury's density profile with the present day mass, polar moment of inertia factor (MOI), the outer shell MOI, and the radial contraction of Mercury. Additionally, they used the 3<sup>rd</sup> order Birch-Murnaghan EoS to determine the thermodynamic parameters of Mercury's core in their models. Their results predicted the outer core radius is between 1985–2090 km, and the inner core radius is less than 1454–1690 km depending on the concentration of the light element in the core. They suggest that the FeS layer at the core (if it exists) is denser than previously thought and requires another mechanism to sustain the FeS layer within the core.

*Peterson et al.* (2021) modified the parameterized mantle convection model used for Mercury by incorporating a volcanic heat-pipe heat flux into the stagnant-lid calculation, and a calculation of entropy sources and sinks within the core to account for ohmic dissipation in the core. They also included a calculation of the stresses experienced by the elastic membrane within Mercury's lithosphere, as this would affect the contraction of the planet. Finally, they accounted for the partitioning of water and radioactive elements in the partial melts formed in Mercury's mantle. However, they do not account for an inner core nucleating or evolving in the core using an inner core melt curve and adiabat, but rather through an assessment of the overpressure in the core. Their results suggested that Mercury's mantle cooled early on due to crustal production via volcanism, which allowed for an inner core to form later leading to the modern magnetic field observed today. They also found that heat lost from the mantle during the early evolutionary stages

is not only influenced by solid state mantle convection, but also by the path of magmatic melts within the mantle from generation to ascent to eruption onto the planet's surface.

The model in this study utilizes model components from these prior investigations of Mercury's thermochemical evolution to holistically model Mercury's thermochemical evolution and investigate potential initial conditions for Mercury. The use of the geochemically relevant (Fe-free) mantle melt parameterization provides a more realistic approximation of the evolutionary path Mercury experienced to reach its present day condition. Thus, by investigating the present day conditions resulting from model runs where the initial conditions were varied, the present day state of Mercury can be used to constrain the initial conditions that Mercury experienced.

By testing a range of initial conditions, the results of the model can be compared to Mercury-relevant constraints that stem from the data from the MESSENGER mission. These constraints are the polar MOI ( $0.346 \pm 0.009$ ; *Margot et al.*, 2012), the mass of the planet ( $3.301110 \pm 0.00015 \times 10^{27}$  kg; *Margot et al.*, 2018), the presence of an inner core with a maximum radius of  $1325 \pm 250$  km (*Breuer et al.*, 2015; *Dumberry and Rivoldini*, 2015), and a total contraction estimate of 2–7 km after the Late Heavy Bombardment ends around 3.8 billion years ago (*Byrne et al.*, 2014; *Claeys and Morbidelli*, 2015; *Watters*, 2021). These constraints indicate which models from this study are successful at replicating Mercury's present day conditions, and which conditions are not.

## 2.2. Thermochemical Evolution Model Description

### 2.2.1. Model Setup

Our 1D thermochemical evolution model of Mercury was built in Python following the model setup from *Grott et al.* (2011). The model will be archived and will be available on GitHub at the following repository: [https://github.com/Bose-Priya/Thermochem\\_eval\\_Merc](https://github.com/Bose-Priya/Thermochem_eval_Merc). Our model was modified based on the geochemical and geophysical findings from the MESSENGER mission, and uses many of the common Mercury parameters from prior models (**Error! Reference source not found.** and references therein). The specific modifications to the *Grott et al.* (2011) model we implemented were: 1) an evolving inner and outer core density, 2) inner core crystallization with a top-down and a bottom-up approach, both based on sulfur content, and 3) using the more geochemically appropriate mantle solidus (*Namur et al.*, 2016) to track mantle melt evolution. These modifications lead to more realistic predictions of Mercury's thermochemical evolution.

For this study, we assumed that the planet is perfectly spherical, and has four layers: a thin crust, a relatively thin mantle, a large core, and an inner core, if present (**Figure 2-1: Model schematics (left)** A cross-section of Mercury's interior showing the crust, the mantle, and the core partitions, along with the approximate thicknesses of each main layer (*Margot et al.*, 2018). The solid lines represent interfaces between the different partitions of Mercury, while the dashed lines represent the growing thermal boundary layers (TBLs) in the mantle. A representative solid inner core is shown as well. **(right)** A thermal profile through Mercury. The temperature reaches its highest point within the inner core at the inner core liquidus, then decreases throughout the core gradually until it reaches the core-mantle boundary (CMB), where the temperature slightly decreases as it crosses the bottom TBL ( $\delta_b$ ), and then decreases adiabatically from the bottom TBL to the top TBL ( $\delta_t$ ). After the temperature progresses through the top TBL, it rapidly decreases until it reaches the surface. After Figure 1 from *Stevenson et al.* (1983). **Figure 2-1**). The initial model state has a fully differentiated core and mantle (*Hauck et al.*, 2004) with a primordial crustal and regolith thickness following *Grott et al.* (2011), prior to the model run. Therefore, the model accounts for heat fluxes in the core and mantle and tracks the thermal energy from the center of the planet outward as the planet cools.

The thermal model tracks this thermal energy using four ordinary differential equations (ODEs) to represent the thermal energy flowing from the planet's center outward. These ODEs use initial conditions for the initial regolith thickness, primordial crustal thickness, initial stagnant lid thickness, and an initial average mantle temperature (**Error! Reference source not found.**). The initial state of the model, defined by these initial conditions, is required by the model to calculate the planetary evolution of Mercury. An additional model requirement is that the core starts out fully molten (i.e., no inner core is present). These initial conditions were incorporated into the model's ODEs to estimate the thermal evolution of Mercury's mantle. The ODEs used in the model calculate the changes in the temperature at the core-mantle boundary (CMB; Eq. 2-1), the change in the average mantle temperature (Eq. 2-2), the change in the stagnant lid thickness (Eq. 2-3), and the change in the inner core radius with respect to time (Eq. 2-4).

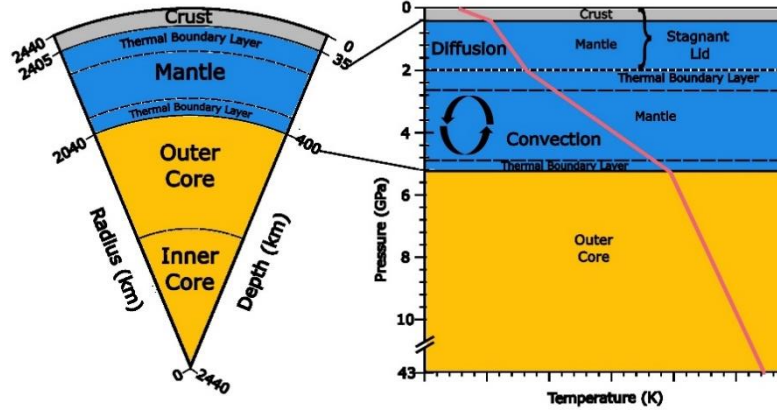


**Figure 2-1:** Model schematics (**left**) A cross-section of Mercury’s interior showing the crust, the mantle, and the core partitions, along with the approximate thicknesses of each main layer (*Margot et al.*, 2018). The solid lines represent interfaces between the different partitions of Mercury, while the dashed lines represent the growing thermal boundary layers (TBLs) in the mantle. A representative solid inner core is shown as well. (**right**) A thermal profile through Mercury. The temperature reaches its highest point within the inner core at the inner core liquidus, then decreases throughout the core gradually until it reaches the core-mantle boundary (CMB), where the temperature slightly decreases as it crosses the bottom TBL ( $\delta_b$ ), and then decreases adiabatically from the bottom TBL to the top TBL ( $\delta_t$ ). After the temperature progresses through the top TBL, it rapidly decreases until it reaches the surface. After Figure 1 from *Stevenson et al.* (1983).

**Table 2-1:** Model Parameters

Parameter	Symbol	Value	Units	Source
Planet Radius	$R_p$	2440	km	a
Core Radius	$R_c$	2020	km	b
Surface Gravity	$g$	3.7	m/s <sup>2</sup>	c
Surface Temperature	$T_s$	440	K	c
Mean/Upper Core Temperature Ratio	$\epsilon_c$	1.1		c
Mantle and Core Temperature Difference	$dT$	200	K	c
Viscosity Reference Temperature	$T_{ref}$	1600	K	c
Crustal Density	$\rho_{cr}$	2800	kg/m <sup>3</sup>	c
Mantle Density	$\rho_m$	3200	kg/m <sup>3</sup>	d
Magma Heat Capacity	$C_{cr}$	1000	J/kg/K	c
Mantle Heat Capacity	$C_m$	1212	J/kg/K	c
Core Heat Capacity	$C_c$	850	J/kg/K	e
Ideal Gas Constant	$R$	8.3144	J/K/mol	c
Universal Gravity Constant	$G$	$6.6726 \times 10^{-11}$	Nm <sup>2</sup> /kg <sup>2</sup>	h
Activation Energy	$A$	$3.0 \times 10^5$	J/mol	c
Mantle Thermal Conductivity	$K_m$	4.0	W/m/K	c
Crust Thermal Conductivity	$K_{cr}$	2.0	W/m/K	f
Regolith Thermal Conductivity	$K_{reg}$	0.2	W/m/K	c
Mantle Thermal Diffusivity	$\kappa$	$1.0 \times 10^{-6}$	m <sup>2</sup> /s	c
Mantle Thermal Expansion Coefficient	$\alpha_m$	$3.0 \times 10^{-5}$	1/K	c
Inner Core Thermal Expansion Coefficient	$\alpha_{c,shrink}$	$5.8 \times 10^{-5}$	1/K	g

Crust Latent Heat of Melting	$L_{cr}$	$6.0 \times 10^5$	J/kg	c
Core Latent Heat of Crystallization	$L_{Eg}$	$2.5 \times 10^5$	J/kg	c
Critical Rayleigh Number	$Ra_{crit}$	450.0		c
Mantle Convection Speed Scale	$u_0$	$2.0 \times 10^{-12}$	m/s	c
Nusselt-Rayleigh Power Law Exponent	$\beta$	1/3		c
Initial Stagnant Lid Thickness	$D_{l0}$	50	km	c
Primordial Crust Thickness	$D_{cr0}$	5	km	c
Initial Regolith Thickness	$D_{reg}$	4	km	g
Fraction of Extractable Crust	$f_c$	0.4		c
Volume Change Upon Differentiation	$\partial V/V$	0.02		
Frank-Kamenetskii Parameter	$\theta$	2.9		f
Pressure Dependence Factor for Viscosity	$f_P$	1		
Crust Enrichment Factor	$V$	4.0		c
Present Day U Surface Abundance	$U_{ppb}$	$90 \times 10^{-9}/V$	ppb	i
Present Day Th Surface Abundance	$Th_{ppb}$	$155 \times 10^{-9}/V$	ppb	i
Present Day K Surface Abundance	$K_{ppm}$	$1288 \times 10^{-6}/V$	ppm	i

a (Perry et al., 2011); b (Margot et al., 2018); c (Grott et al., 2011); d (Lark et al., 2022); e (Berrada et al., 2021); f (Morschhauser et al., 2011); g (Grott, 2022); h (Turcotte and Schubert, 2002); i (Nittler et al., 2018)

Assuming each layer is in hydrostatic equilibrium with the next, the pressure at the base of each layer was calculated with an integration given the radial bounds for the respective layer. These radial bounds are the base of the crust, the CMB, and the inner core boundary (ICB), which are summed to find the central pressure. We assumed constant density and gravity values for the crust and mantle, as the thicknesses of these layers are relatively thin when compared to the radius of the planet. Due to the large size of the core, the densities of solid Fe and liquid FeS were not considered constant and are calculated at each timestep, along with the gravity profile in each layer (Turcotte and Schubert, 2002). To maintain a self-consistent inner core calculation, the model determines the pressure at the CMB and the ICB, and the pressure profiles through the inner and outer core. The sum of these pressures was used as the central pressure of the core for each timestep. The calculated central pressure value was set as one end of a pressure array, while the other end was the pressure at the CMB. This pressure array was used to calculate the core's adiabat (Stevenson et al., 1983) and melt curve (Rivoldini et al., 2011) temperatures.

A crustal enrichment factor of 4 was utilized for our model, as it falls within the range of crustal enrichment constants computed by (Tosi et al., 2013) in multiple Monte Carlo runs with various core sizes for Mercury. Following the logic in (Grott et al., 2011) and (Michel et al., 2013), the Frank-Kamenetskii approximation was used for the rheology and the viscosity contrast at the

base of the stagnant lid was set to 2.9, because mantle convection occurs under a stagnant lid, and is driven by the rheological temperature scale (*Reese et al.*, 1998).

The condition of Mercury after formation, i.e., its initial condition, is not well constrained. Therefore, we varied the initial mantle temperature, mantle reference viscosity, and initial core sulfur content (Error! Reference source not found.). We varied mantle temperature from 1600–1900 K, allowing us to test a range of initial conditions, similar to previous studies (*Grott et al.*, 2011; *Hauck et al.*, 2004; *Michel et al.*, 2013). The mantle viscosity depends on the mineralogy, likely orthopyroxene, clinopyroxene, olivine, and garnet, which are common in the terrestrial planets. Of these minerals, olivine is thought to be the weakest mineral and is used to calculate the flow laws for the Mercurian mantle, as is done for Earth (*Katayama*, 2021; *Mackwell*, 1991). The reference viscosity was varied from  $10^{19}$ – $10^{22}$  Pa s based on an olivine rich mantle (*Karato and Wu*, 1993), while clinopyroxene deformation experiments indicate that the viscosity for a clinopyroxene dominated mantle is between  $10^{20}$ – $10^{22}$  Pa s. Initial core sulfur content was varied from 0.5 wt.% S to 8.9 wt.% S, as the outer core becomes enriched with S with the formation and growth of the solid inner core, since no S partitions into the solid inner core (*Breuer et al.*, 2015; *Chabot et al.*, 2014; *Hemingway and Driscoll*, 2021; *Li et al.*, 2001; *Pommier*, 2018; *Wicht and Heyner*, 2014). As the current S concentration is the estimate of S in the outer core after the inner core formed, it is logical to limit the S range to 8.9 wt.% (in the event of no inner core forming at all). A minor amount of S in the core was used as the low end of the initial core S concentration, because no S input into the core would lead to a pure Fe outer core, and causes instability in the model.

**Table 2-2:** Varied Parameters in the Model

Parameter Name	Symbol	Range	Units
Initial Mantle Temperature	$T_{m0}$	1600–1900 K	
Mantle Reference Viscosity	$\eta_{ref}$	$10^{19}$ – $10^{22}$ Pa s	
Initial Core S Content	$X_0$	0.5–8.9	wt.% S

### 2.2.2. The Core

As with other prior thermochemical models (*Grott et al.*, 2011; *Hauck et al.*, 2004; *Hauck et al.*, 2013; *Knibbe and van Westrenen*, 2015; *Michel et al.*, 2013; *Peterson et al.*, 2021; *Rivoldini and Van Hoolst*, 2013; *Stevenson et al.*, 1983; *Tosi et al.*, 2013), the core is considered to be adiabatic because it is assumed there are no heat producing elements in the core (*Williams*, 2009).

The model tracks the heat flow in the core by calculating the change in the CMB temperature with time. At the initial time step of the model, the temperature at the CMB was found using the mantle adiabat equation:

$$T_{c0} = T_{m0} + dT + \frac{\alpha_m g T_{m,0}}{C_m} (R_p - D_{l0} - R_c) \quad (2-1)$$

where  $T_{m,0}$  is the input mantle temperature for the model,  $dT$  is the temperature offset between the mantle and core (due to the thermal profile increasing with depth),  $\alpha_m$  is the thermal expansion coefficient for the mantle,  $C_m$  is the specific heat of the mantle,  $R_p$  is the radius of the planet,  $D_{l0}$  is the initial depth of the stagnant lid, and  $R_c$  is the radius of the planet's core. The temperature at the CMB was calculated in this manner because the mantle was assumed to have an adiabatic thermal profile. This method also eliminates most of the uncertainty that would be in the model if an initial CMB temperature value was preset for the model.

The temperature at the CMB is dependent on the energy balance at the CMB and is given by:

$$\frac{dT_c}{dt} = \frac{-q_c A_c}{\rho_{FeS} C_c Vol_c \epsilon_c - L_{eg} A_{ic} \rho_{Fe} \frac{dR_i}{dT_{cm}}} \quad (2-2)$$

where  $q_c$  is the core heat flux,  $A_c$  is the core area ( $A_c = 4\pi R_c^2$ ),  $\rho_{FeS}$  is the core density in the liquid portion of the core,  $C_c$  is the core specific heat,  $Vol_c$  is the core volume ( $Vol_c = \frac{4}{3}\pi R_c^3$ ),  $\epsilon_c$  is the ratio between the temperature at the top of the core and the average core temperature. The second term in the denominator represents the removal of heat in the fluid portion of the core where  $L_{eg}$  is the energy release during core formation,  $A_{ic}$  is the area of the inner core ( $A_{ic} = 4\pi R_{ic}^2$ ),  $\rho_{Fe}$  is the density of the solid inner core, and  $\frac{dR_i}{dT_{cm}}$  is the rate of change in the inner core radius with respect to the CMB temperature.

The heat flow throughout the entire planet depends on the heat flow from the core either explicitly or implicitly because Mercury is in a steady state. The core heat flux is impacted by the change in the size of the inner core. This change in the size of the inner core is calculated with a finite-difference method over a set of realistic CMB temperatures, and this is interpolated with the CMB temperature of the iteration to obtain the  $\frac{dR_i}{dT_{cm}}$  term, all other terms in the model are the same as described above:

$$\frac{dR_i}{dt} = \frac{-q_c A_c \frac{dR_i}{dT_{cm}}}{\rho_{FeS} C_c Vol_c \epsilon_c - L_{eg} A_{ic} \rho_{Fe} \frac{dR_i}{dT_{cm}}} \quad (2-3)$$

We tracked the thermal energy within Mercury’s interior, which is strongly influenced by the evolution path Mercury experienced. The amount of mantle melting, the growth of the inner core, and the growth of the crust all impact the amount of heat that flows throughout the planet.

### 2.2.2.1.Core Density

For this model, the core is assumed to have an Fe+S composition, as in previous work (*Dumberry and Rivoldini, 2015; Grott et al., 2011; Michel et al., 2013*). During inner core formation, S will preferentially remain in the liquid portion of the core, while Fe partitions into the solid portion of the core. Thus, it is assumed the solid core is composed of pure Fe. The evolution of the S content in the liquid core as the solid core grows significantly affects the densities of the solid Fe and liquid FeS. Thus, these densities were updated during each iteration of the run to ensure the core’s composition at that iteration is consistent with the densities used in the calculation of the CMB temperature and inner core radius.

Average inner and outer core densities were calculated using the 3<sup>rd</sup> order Birch-Murnaghan EoS:

$$P = \frac{3}{2}K_T \left[ \left( \frac{\rho}{\rho_0} \right)^{\frac{7}{3}} - \left( \frac{\rho}{\rho_0} \right)^{\frac{5}{3}} \right] \left\{ 1 + \frac{3}{4}(K' - 4) \left[ \left( \frac{\rho}{\rho_0} \right)^{\frac{2}{3}} - 1 \right] \right\} + \alpha K_T (T - T_0) \quad (2-4)$$

where  $K_T$  is the bulk modulus,  $\rho_0$  is the reference density,  $\rho$  is the density at a given pressure,  $K'$  is the pressure derivative of the bulk modulus,  $\alpha$  is the thermal expansion coefficient,  $T$  is the adiabatic temperature value, and  $T_0$  is the reference temperature. We used a similar procedure as *Knibbe and van Westrenen (2015)* with the same values for solid Fe (*Komabayashi and Fei, 2010*), and liquid FeS (*Jing et al., 2014; Sanloup et al., 2000*). The calculated densities for solid Fe were averaged over the pressure range of the inner core as a function of S content, and fit to a line (**Figure B-1**) to be easily updatable at each model timestep:

$$\rho_{FeS} = -13316X_S + 8417.4 \quad (2-5)$$

$$\rho_{Fe} = -0.2855 \left( \frac{P}{10^9} \right)^2 + 54.778 \left( \frac{P}{10^9} \right) + 7190.9 \quad (2-6)$$

where  $X_S$  is the mass fraction of S within the core, and the  $P$  is the core pressure profile in Pa.

### 2.2.2.2.Inner Core Crystallization Methods

We used a different approach to calculate the inner core formation and growth than any of the previous studies by accounting for inner core crystallization from the top-down and bottom-up, as well as the changing densities of Fe and Fe+S caused by the growth of a solid portion of the

core. The prior models (*Grott et al., 2011; Hauck et al., 2004; Michel et al., 2013; Tosi et al., 2013*) assumed an inner core growth mechanism of bottom-up core crystallization. The melt curve used for the core, taken from (*Rivoldini et al., 2011*), accounts for the shifting eutectic composition as a function of pressure, which is manifested as a step wise formulation at higher sulfur contents (Appendix B). This allows for intersections of the melt curve and adiabat near the top of the core, with the upper layer solidifying first: top-down crystallization, rather than the more common bottom-up crystallization, or some combination of the two. To account for this accurately in the model, we devised a workflow (**Figure 2-2**) that describes the method of calculating the radius of the inner core given either pathway. Core crystallization from the top-down was proposed for Mercury, and other small bodies in the Solar system such as Ganymede and the Moon (*Hauck et al., 2006; Hauck et al., 2018; Hemingway and Driscoll, 2021; Jing et al., 2014; Pommier, 2018; Rückriemen et al., 2018; Vilim et al., 2010; Williams, 2009*). In the top-down cases, the Fe snow falls to the planet’s center without remelting, based on the relative densities of solid Fe and liquid Fe+S and the relative locations of the core adiabat and the Fe melt curve.

As the inner core can crystallize from the top-down or the bottom-up, both cases are considered here. Because the core adiabat and the core melt curve are calculated over a pressure array from the center of the planet to the CMB, the intersection location between the two temperature curves will indicate the method of inner core solidification. To determine where the intersection(s) occurs, the sign of the difference between the core adiabat and melt curve is observed and the location(s) where the sign switches from negative to positive and then positive to negative is where the intersection begins and ends. The negative value indicates the core is entering the intersecting region, while a positive value indicates the core is exiting the intersecting region. This sign change is based on the first value in the difference array which is set to either 0 or 1. If the first value is 0, a solid inner core is forming from the center outwards. If the first value is 1, the core has the potential for Fe snow crystallization. Depending on the location(s) of the intersection(s), one of two paths are followed, and are described below.

The pressure of the ICB ( $P_{ioc}$ ) was found by determining the intersection of the core adiabat (*Stevenson et al., 1983*) and the Fe+S melt curve (*Rivoldini et al., 2011*), using the pressure array discussed above. Using the pressure of the intersection, the radius of the intersection ( $R_{int}$ ) was calculated, which represents the inner-outer core boundary (bottom-up approach), or the base of the snow zone (top-down approach). For the bottom-up approach, the radius of the inner core is

found by rearranging the hydrostatic pressure equation with the gravity term representing the gravity in a sphere of constant density (*Grott et al.*, 2011; *Grott*, 2022):

$$R_{int} = R_{ic} = \sqrt{\frac{3(P_c - P_{ioc})}{2\pi\rho^2G}} \quad (2-7)$$

where  $P_c$  represents the central pressure in Pa,  $\rho$  is the density of the inner core: solid Fe in the bottom-up cases and liquid Fe+S in the top-down cases, and  $G$  is the universal gravitation constant.

To ensure all core parameters are consistent with this newly found inner core radius, the calculated radius is used to recalculate the sulfur mass fraction for the liquid outer core, which updates the densities of the liquid Fe+S outer core, and the central core pressure. As a check for convergence, the sum of the overlying pressures of the inner core (the recalculated mantle and outer core pressures) was subtracted from the pressure at the inner-outer core boundary. If this is a small value (<10 Pa), the calculated inner core radius is accepted. If the difference is greater than 10 Pa, then the inner core radius is adjusted by the change in radius calculated using the derivative of the pressure equation with respect to radius. The radial adjustment is repeated until the radius difference is <10 Pa, after which it is taken as the calculated inner core radius for that step, and convergence is achieved.

However, if top-down crystallization occurs in the core,  $R_{int}$  represents the base of the snow zone and not the boundary of the inner core. Above this radius, solid Fe can crystallize as Fe-snow within the snow zone, and the mass of the Fe snow must be determined so an equivalent volume can be added to the inner core (if it already exists). To obtain a snow zone, the core melt curve temperature must be less than the core adiabat temperature within a section of the core (between  $R_{int}$  and the top of the intersecting region). The core snow zone can start at any radius above the base of the snow zone (i.e., the CMB radius or any radius below it), and is denoted by  $R_{o,int}$  if it exists within the core. If the top intersection is not greater than the CMB pressure, it is assumed that  $R_{CMB}$  is the top intersection point. The code calculates the intersection(s) of the core adiabat and melt curve and converts these pressures into radii using a modified version of the equation for the inner core radius (Eq. 2-7).

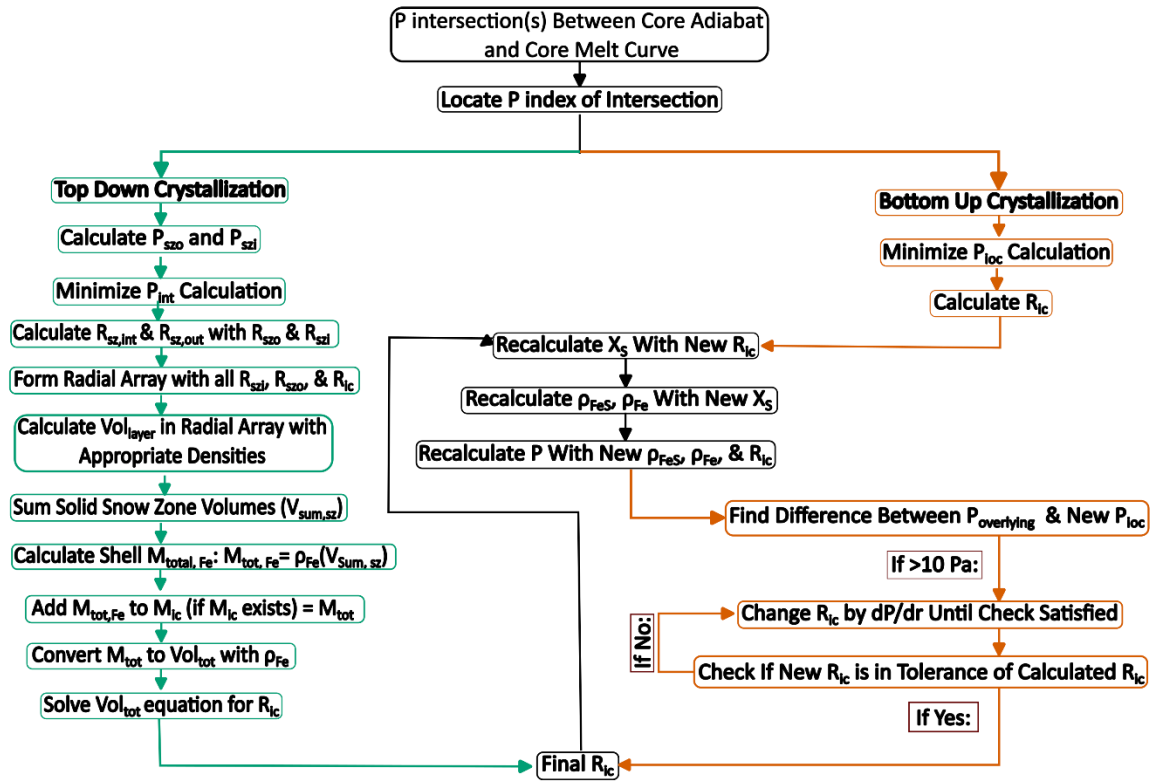


**Figure 2-2:** The method used to calculate inner core crystallization. Based on the updated melting curve from Rivoldini *et al.* (2011), both top-down and bottom-up core crystallization processes are possible for Mercury. The green lines indicate the steps to calculate the inner core crystallization using the top-down core crystallization approach, and the orange lines denote the steps to calculate the inner core crystallization using the bottom-up core crystallization approach. Steps that are used in both approaches are shown in black, and the pathways are described in the text.

Once the radii of the snow zone(s) is(are) found, the shell volume is calculated using the volume of a shell equation and converted to a mass by multiplying the shell volume by the calculated density of solid Fe. The total solid Fe mass in the core is found by adding the calculated Fe mass from the snow zone to the (already existing) inner core mass and converted into a total inner core volume by dividing the total Fe mass by the calculated density of solid Fe. The simple geometric volume equation for a sphere is rearranged to calculate the radius of the new inner core. In the Fe-snow regime, the last 10 shell volumes and inner core radii are recorded, and a check for convergence is done on both values. For both sets of 10 values, convergence is assumed if the standard deviation of the set is less than a millionth of the mean of the set or if the standard deviation of the set is less than one. The calculation is repeated until the convergence criteria is met.

### 2.2.3. The Mantle

Understanding the mantle evolution within Mercury requires knowledge of the mantle composition and an estimate of the heat flowing through the mantle. Mantle composition controls the abundance of heat producing elements (HPEs) and mantle melting, which in turn affects how heat is transferred. The initial heat within Mercury comes from residual heat from Mercury's formation and the decay of the initial abundances of HPEs within Mercury's mantle:  $^{235}\text{U}$ ,  $^{238}\text{U}$ ,  $^{232}\text{Th}$ , and  $^{40}\text{K}$  (Schubert, 2006; Tosi and Padovan, 2021). This internal heat must dissipate throughout the planet's entirety and is eventually released from the planet's surface. Because Mercury is in a stagnant lid regime (Breuer *et al.*, 2015; Grott *et al.*, 2011; Hauck *et al.*, 2004; Hauck *et al.*, 2018; O'Neill *et al.*, 2007; Stern *et al.*, 2018), plate tectonics is not an appropriate mechanism to cool the interior of Mercury. Thus, Mercury relies on planet cooling only convection or conduction to transport heat from the center of the planet out to space over 4.5 Gyr. The heat flow in Mercury's interior dictates what processes occur within the planet. Formation of partial melt within the mantle is possible if the mantle adiabat is greater than the mantle solidus. Mantle melt formation is a significant source of heat release from Mercury's interior, and depends on the composition of the mantle.

The modeled mantle has two thermal boundary layers (TBLs): one located at the base of the stagnant lid (at the top of the convecting mantle), and one located at the base of the convecting mantle above the core (**Figure 2-1**). These layers are where heat is transported via conduction rather than convection. As the total heat flow through the mantle decreases, the mantle cools over time, causing the TBLs to grow, which effectively shrinks the convective region within the mantle, and eventually meet in the middle (Grott *et al.*, 2011). The growing TBLs make mantle convection less efficient (Hauck *et al.*, 2018), and as such decreases the Rayleigh number, which leads to a switch of cooling mechanism in the mantle from convection to conduction. To calculate the thickness of the bottom TBL, the gravity at the CMB was found using the gravity acceleration equation for a spherically symmetric body (Turcotte and Schubert, 2002), and accounting for mass of the inner and outer cores within this calculation.

As the mantle cools, it grows a uniform stagnant lid, equivalent to the rheological lithosphere of the planet (Schubert *et al.*, 1979; Schubert and Spohn, 1990; Spohn and Schubert, 1982; Spohn, 1991). Crustal growth, described below, causes the stagnant lid to thermally erode and the eroded material is assumed to be recycled into the mantle (Grott *et al.*, 2011; Morschhauser

*et al.*, 2011). This is described as the heat piping method of magma transport, and is assumed to effectively transport heat from the mantle through the stagnant lid, balancing the incoming core heat flux as in *Morschhauser et al.* (2011) and *Grott et al.* (2011). The growth of the stagnant lid is calculated by:

$$\frac{dD_l}{dt} = \frac{-q_l + C_{melt} \frac{dD_{cr}}{dt} - K_m \frac{dT}{dr}}{\rho_m C_m (T_m - T_{bsl})} \quad (2-8)$$

where  $K_m$  is the thermal conductivity of the mantle, and  $\frac{dT}{dr}$  is the thermal profile through the solid outer shell (from the surface of the planet to the core radius). The derivation of the thermal profile is described in the appendix based on personal communication with *Grott* (2022).

The mercurian mantle has a heat flux input from the core, so the model assumes that the mantle has bottom heated convection (*Hauck et al.*, 2018), which passes heat from the core, through the mantle and crust to the surface of the planet. As the mercurian mantle convects, a global melt zone region forms, in which partial melt can be generated. It is assumed this melt is extracted instantly for the sake of simplicity in the model, and mantle convection remixes the melt with the undepleted mantle material (*Hauck et al.*, 2018). The mantle heat flow is tracked by calculating the change in the mantle temperature with time, which affects the generation of partial melt. Prior to the start of the simulation (i.e., before any mantle melting or lid growth occurs), the volume of the silicate shell is calculated (from the radius of the core to the surface of the planet). The thermal energy from the core goes into the mantle and is tracked with the ODE that calculates the mantle's average temperature:

$$\frac{dT_m}{dt} = \frac{-(q_l + C_{melt} \frac{dD_{cr}}{dt}) A_l + q_c A_c + Q_m Vol_m}{\rho_m C_m Vol_l \epsilon_m (1 + St)} \quad (2-9)$$

where the numerator accounts for the heat moving through the stagnant lid: heat flux ( $q_l$ ), the mantle melt removal via heat piping to form the crust ( $C_{melt}$ ), the change in the crustal thickness ( $\frac{dD_{cr}}{dt}$ ), the area of stagnant lid ( $A_l = 4\pi R_l^2$  with  $R_l$  as the radius of the stagnant lid); the heat flux entering the mantle from the core ( $q_c$ ), the area this heat flux acts over ( $A_c$ );  $Q_m$  represents the volumetric heat rate from the radiogenic elements decaying, and  $Vol_m$  represents the volume of the convecting mantle ( $Vol_m = \frac{4}{3}\pi(R_l^3 - R_c^3)$ ). The denominator accounts for the phase change in the mantle from melt to solid as the mantle cools, with  $\rho_m$  and  $C_m$  representing the mantle density and heat capacity, respectively,  $Vol_l$  is the volume of the convecting mantle,  $\epsilon_m$  is the adiabatic correction factor for the mantle, and  $St$  is the Stefan number, which accounts for the phase

transition occurring within the mantle as the convective mantle decreases and the stagnant lid depth increases using equation (2) from *Morschhauser et al. (2011)*. The heat piping term is expanded:

$$C_{melt} = \rho_{cr}C_{cr} + \rho_{cr}C_{cr} (T_m - T_{bsl}) \quad (2-10)$$

where  $\rho_{cr}$  and  $C_{cr}$  are the density and specific heat of the crust respectively,  $T_m$  represents the average temperature of the mantle, and  $T_{bsl}$  represents the base of the stagnant lid.

The heat flux leaving the mantle is found by taking the change in temperature across the top TBL, dividing it by the thickness of the top TBL and multiplying it by the mantle's thermal conductivity. This heat flux enters the stagnant lid from the mantle and is diffused to the surface of the planet:

$$q_l = K_m \frac{T_m - T_{bsl}}{\delta_t} \quad (2-11)$$

The heat flux entering the mantle from the core is found in an analogous manner. The temperature difference between the CMB and the bottom of the convecting mantle ( $T_{bcm}$ ) is divided by the bottom TBL thickness, and multiplied by the mantle's thermal conductivity:

$$q_c = K_m \frac{T_c - T_{bcm}}{\delta_b} \quad (2-12)$$

How strongly the mantle convects is dependent on the viscosity of the mantle. Following the methodology of *Grott et al. (2011)*, the mantle viscosity is found via:

$$\eta_m = \eta_{ref} e^{\frac{A(T_{ref} - T_m)}{R(T_{ref} T_m)}} \quad (2-13)$$

where a reference viscosity ( $\eta_{ref}$ ) and temperature ( $T_{ref}$ ) values (**Table 2-2**), with  $T_m$  as the timestep specific mantle temperature. Viscosity is a key component for the mantle Rayleigh number ( $Ra_m$ ), which calculates the ratio between diffusion and convection time scales in the mantle:

$$Ra_m = \frac{\rho_m g \alpha_m (T_m - T_{bsl} + T_c - T_{bcm}) (R_l - R_c)^3}{(\eta_m \kappa)} \quad (2-14)$$

where  $\alpha_m$  is the thermal expansivity of the mantle,  $g$  is the surface gravity value,  $T_c$  is the temperature at the CMB,  $T_{bcm}$  is the temperature at the bottom of the convecting mantle,  $R_c$  is the radius of the CMB,  $\eta_m$  is the viscosity of the mantle, and  $\kappa$  is the mantle thermal diffusivity. The critical Rayleigh number was set to 450 (*Grott et al., 2011*). Using boundary layer theory (*Turcotte and Schubert, 2002*), the thicknesses of the top and bottom TBLs within the mantle were calculated (Appendix C).

### 2.2.3.1. Mantle Melting

Prior thermochemical evolution models used the peridotite solidus to calculate mantle melting (*Grott et al.*, 2011; *Hauck et al.*, 2004; *Michel et al.*, 2013; *Tosi et al.*, 2013). This solidus is too iron-rich, and does not reflect the lower iron content of Mercury's mantle (*Nittler et al.*, 2018; *Vander Kaaden et al.*, 2017; *Weider et al.*, 2012). The solidus derived by *Namur et al.* (2016) from Mercury's surface lava compositions, better reflects the bulk composition of Mercury's mantle. We used both mantle solidi in our model to determine the significance of the difference between the two melting parameterizations, but the Fe-free melt parameterization is used in the model to obtain more realistic estimates of Mercury's evolution conditions. We parameterized the peridotite solidus ( $T_{sol,T}$ ) and liquidus ( $T_{liq,T}$ ) from previous experiments (*Takahashi*, 1990):

$$T_{sol,T} = -4.7911P^2 + 127.55P + 1403.55 \quad (2-15)$$

$$T_{liq,T} = -2.5245P^2 + 55.608P + 2031.75 \quad (2-16)$$

while the Fe-free solidus ( $T_{sol,N}$ ) was provided by *Namur et al.* (2016) and we fit a liquidus ( $T_{liq,N}$ ) equation fitted from their Figure 6:

$$T_{sol,N} = -12.2P^2 + 177P + 1421.15 \quad (2-17)$$

$$T_{liq,N} = 0.1166P^2 + 69.215P + 1931.35 \quad (2-18)$$

While the *Namur et al.* (2016) equation was used by *Padovan et al.* (2017) to account for mantle melting, they only focused on the additional melting that would occur after impacts to understand how impacts affected the crustal thickness, and not how this composition affects the thermochemical evolution of Mercury.

For each run, the mantle solidus and liquidus temperatures were compared to the thermal profile of the mantle, constrained by the adiabat (*Stevenson et al.*, 1983) to determine the melt zone, or amount of partial melt generated during each iteration of the model. If melt formation is possible, the melt fraction is calculated over the radial array of the silicate shell from the bottom of the mantle to the base of the crust, with  $T_{prof}$  as the mantle thermal profile, where resulting values were between 0 and 1:

$$F = \frac{T_{prof} - T_{sol}}{T_{liq} - T_{sol}} \quad (2-19)$$

Then, the volumetrically averaged degree of melting ( $M_{deg}$ ) was determined. The volumetrically averaged melt zone ( $Vol_{mz}$ ) is bounded by the radius of the melt zone ( $R_{mz}$ ) and the radius of the

lid ( $R_l$ ), as melt can only form between  $R_{mz}$  and the base of the stagnant lid. For ease of computation, the volumetric integral was converted into a radial integral:

$$M_{deg} = \frac{1}{Vol_{mz}} \int_{R_{mz}}^{R_l} 4\pi R^2 F dr \quad (2-20)$$

The derivative of the volume-averaged degree of melting was computed by repeating the same calculation with a 99% similar thermal profile and a finite difference calculation was performed. This term is required for the calculation of the Stefan number, used to determine the mantle's ratio of sensible heat to latent heat that changes due to phase changes in the mantle. The Stefan number is calculated as follows:

$$St = \frac{L_{cr} Vol_{mz}}{C_m Vol_m} \frac{dM_{deg}}{dt} \quad (2-21)$$

where  $L_{cr}$  is the latent heat of the mantle melting for crustal production,  $C_m$  is the specific heat of the mantle,  $Vol_{mz}$  is the volume of the melt zone (found with the radius of the melt zone),  $Vol_m$  is the volume of the mantle, and  $\frac{dM_{deg}}{dt}$  is the change in the volumetrically averaged melt degree with time. Mantle melting is an efficient mechanism for the planet to lose some of its internal heat. The more heat removed from the mantle due to mantle melt generation allows the core to cool more efficiently and leads to a greater possibility of an inner core forming.

#### 2.2.4. The Crust

Within the model, the crust is located atop a uniform stagnant lid described above. Crustal growth occurs when partial melt, rises via heat-piping from the melt zone and erupts on the surface forming the crust (*Peterson et al.*, 2021). As the crust is assumed to be homogeneously enriched in radioactive elements (*Grott et al.*, 2011; *Hauck et al.*, 2004; *Michel et al.*, 2013), and has a low thermal conductivity (*Hauck et al.*, 2004), the crust acts as an insulator for the stagnant lid and mantle. The low thermal conductivity (*Morschhauser et al.*, 2011) restricts the heat flowing through the crust, compared to the mantle, thus leading to an insulation of the stagnant lid and mantle. The crustal growth rate changes with time and is calculated by:

$$\frac{dD_{cr}}{dt} = u M_{deg} \frac{Vol_{mz}}{4\pi R_p^3} \quad (2-22)$$

where  $u$  is the mantle convection speed (Appendix C),  $M_{deg}$  is described above,  $Vol_{mz}$  is the volume of the melt zone, and  $R_p$  is the radius of the planet.

### 2.2.5. Planetary Contraction

As the planet evolves, the planet's radius can change due to secular cooling, inner core formation, and crustal production. Of these three factors, both secular cooling and inner core formation cause the planet to contract while the production of crust causes the radius of the planet to expand (*Grott et al.*, 2011; *Hauck et al.*, 2018).

Following the methodology of *Grott et al.* (2011), the radial change due to secular cooling is calculated by accounting for the change in the thermal structure of the planet at any time greater than planet formation ( $t = 0$  years), and the initial thermal structure is integrated over the radial profile to obtain the volume change caused by the thermal change (their equation 5). To account for the effect the inner core growth, a new term is introduced: the inner core thermal expansivity coefficient ( $\alpha_{c,shrink}$ ). The radial change due to secular cooling is calculated with:

$$\Delta R_{th} = \frac{1}{R_p^2} \left[ \int \alpha_m (T_{prof} - T_{0,prof}) r^2 dr + \alpha_{c,shrink} \left( \frac{R_c^3}{3} \right) (T_{cm} - T_{c,0}) \right] \quad (2-23)$$

where the first term on the right hand side after the integral accounts for the cooling of the mantle while the term after the plus sign accounts for the secular cooling of the core,  $T_{prof}$  is the current temperature profile of the silicate part of the mantle calculated per each model iteration,  $T_{0,prof}$  is the initial temperature profile of the silicate part of the planet at time = 0 yrs., and  $r$  is the radial profile in the silicate part of the planet,  $T_{cm}$  is the temperature at the CMB for the current iteration of the model run, and  $T_{c,0}$  is the initial CMB temperature.

The radial change caused by the formation of the inner core is computed following *Grott et al.* (2011):

$$\Delta R_{ic} = \frac{\rho_{FeS} - \rho_{Fe}}{\rho_{FeS}} \left( \frac{R_i^3}{3} - \frac{R_p^3}{3} \right) \quad (2-24)$$

As the formation of an inner core is a mechanism of planet cooling, the growth of the inner core causes the planet to shrink with time.

Crustal growth changes the extent of the silicate part of Mercury, and results from the volume change upon differentiation  $\left( \frac{\delta V}{V} \right)$  assumed in the code. For this study, the value of  $\frac{\delta V}{V}$  was found using the equation 16 from *Grott et al.* (2011) with the ratio of extrusive to intrusive volcanism set at 10% following the logic from *Padovan et al.* (2017):

$$\Delta R_{md} = \frac{1}{f_c} \frac{\delta V}{V} (D_{cr} - D_{cr,0}) \quad (2-25)$$

where  $f_c$  is the fraction of extractable crust,  $D_{cr}$  is the thickness of the crust during the current iteration, and  $D_{cr,0}$  is the initial thickness of the crust.

## 2.3. Results

First, we compared our changes of variable core density and updated core melting curve, and Fe-free mantle melting curve to the previous model by *Grott et al.* (2011). Then we varied three model inputs: the initial core S content, the initial mantle temperature ( $T_{m,0}$ ), and the mantle reference viscosity ( $\eta_{ref}$ ). The results of these model runs are discussed below, and alternative visualizations of the data are shown in Appendix D. Model results were constrained by the present day Mercury parameters of crustal thickness: 15–53 km (*Padovan et al.*, 2015; *Sori*, 2018), inner core radius: max of  $1325 \pm 250$  km (*Breuer et al.*, 2015; *Dumberry and Rivoldini*, 2015), mass:  $3.301110 \pm 0.00015 \times 10^{23}$  kg (*Margot et al.*, 2018), MOI factor:  $0.346 \pm 0.009$  (*Margot et al.*, 2012), total radial contraction: 2–7 km after the Late Heavy Bombardment ended  $\sim 3.8$  Ga (*Byrne et al.*, 2014; *Claeys and Morbidelli*, 2015; *Watters*, 2021), cessation of mantle melting by 3.7–3.5 Ga (*Byrne et al.*, 2016), and final core S concentration: 2.8–8.9 wt.% S (*Knibbe and van Westrenen*, 2015).

### 2.3.1. Changing Core Density and Melting

To ensure our model produced reasonable results, we tested it with the same input conditions as *Grott et al.* (2011), but with our variable core density and the core melting curve of *Rivoldini et al.* (2011). The input conditions were: a peridotite melt parameterization, an initial  $T_m$  of 1700 K, a 200 K temperature offset between the mantle and CMB temperatures, a  $k_{cr}$  of 2 W/m/K, a  $D_{reg}$  of 4 km, an  $\eta_{ref}$  of  $10^{21}$  Pa s, a volume change upon mantle differentiation of 0.04, an initial core S input of 8 wt.% S, a fixed core radius of 1840 km, which is smaller than the MESSENGER result, and a core specific heat of 465 J/kg/K. The results are close to the *Grott et al.* (2011) results (their Figure 3, our **Figure 2-3**), indicating that our model produces reasonable results for Mercury. The main difference is that the model of *Grott et al.* (2011) forms an inner core (their Figure 3d), while our model does not (**Figure 2-3f**) due to the differences highlighted above. This model will be used as a baseline comparison for our results.

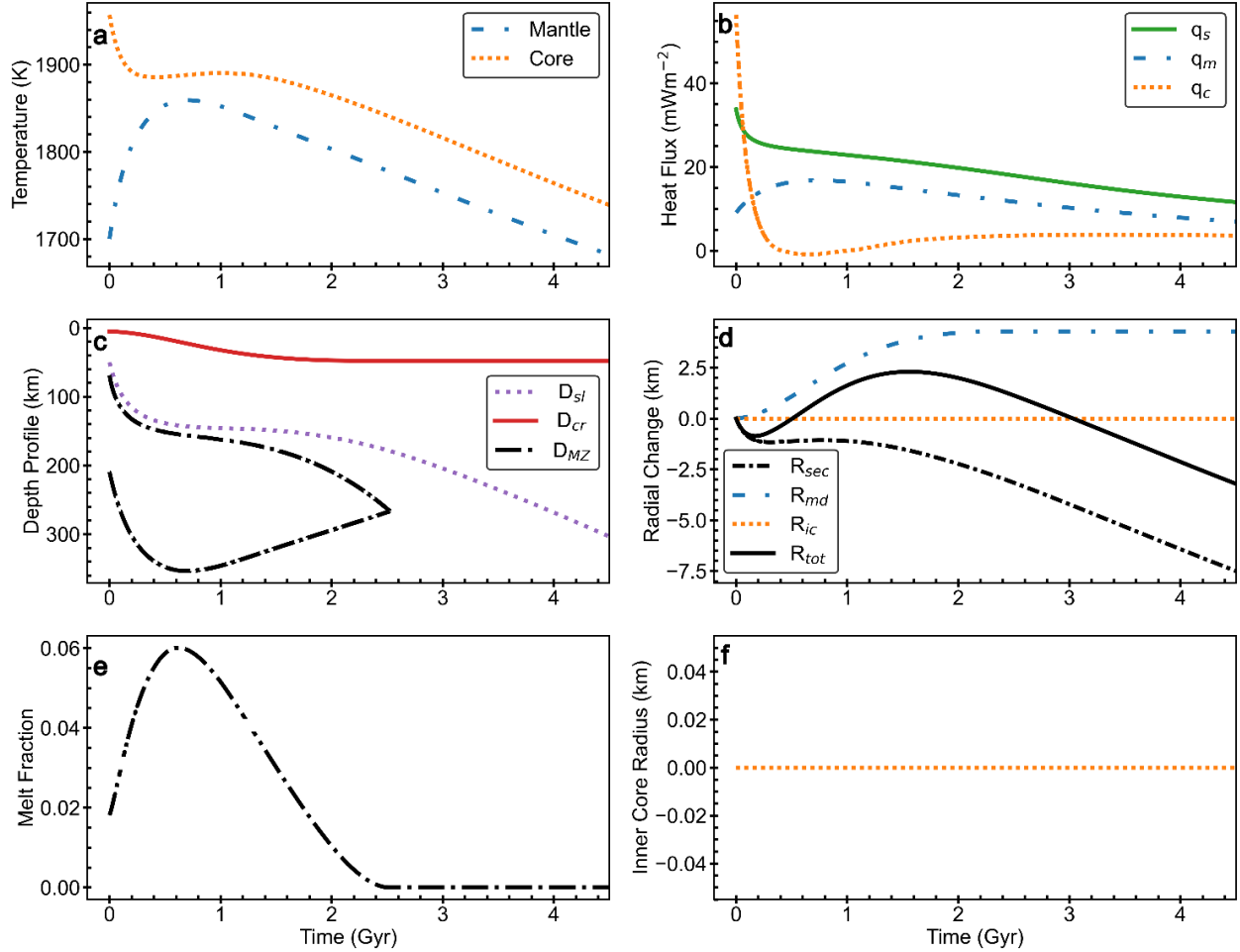


**Figure 2-3:** Model results using a peridotite melt parameterization (*Takahashi, 1990*) and the same inputs as *Grott et al. (2011)* as a function of time. **(a)** Thermal profile of the core (orange dotted line) and the mantle (blue dash dot line). **(b)** Calculated heat fluxes: the core heat flux ( $q_c$  – dotted orange line), the mantle heat flux ( $q_m$  – blue dash dot line), and the surface heat flux ( $q_s$  – solid green line). **(c)** The silicate radial profile: the crustal depth ( $D_{cr}$  – solid red line), the stagnant lid depth ( $D_{sl}$  – dotted purple line), and the melt zone in the mantle ( $D_{mz}$  – black dash dot line). **(d)** Contraction profiles: radial contraction due to inner core formation ( $R_{ic}$  – orange dotted line), due to mantle differentiation ( $R_{md}$  – blue dot dash line), due to secular cooling ( $R_{sec}$  – black dash-dot line), and total planet radial contraction ( $R_{tot}$  – solid black line). **(e)** Calculated volume averaged mantle melt fraction. **(f)** Calculated inner core radius.

### 2.3.2. The Fe-Free Melt Parameterization

We then ran the model with the *Grott et al. (2011)* input conditions, but mantle melting was changed to the more appropriate Fe-free melt parameterization of *Namur et al. (2016)* (**Figure 2-4**). Compared to the model with the peridotite mantle melt parameterization (**Figure 2-3**), the Fe-free melt parameterization (**Figure 2-4**) causes significant differences in model results. The Fe-free melt parameterization results in a 20 K hotter core and mantle at the present day, a slightly greater mantle heat flux of  $0.77 \text{ mW/m}^2$ , 4 km less radial contraction due to mantle differentiation,

~22 km less crustal formation, 50% less mantle melt, and greater secular cooling contribution to radial change of 0.5 km. This model also did not produce an inner core.

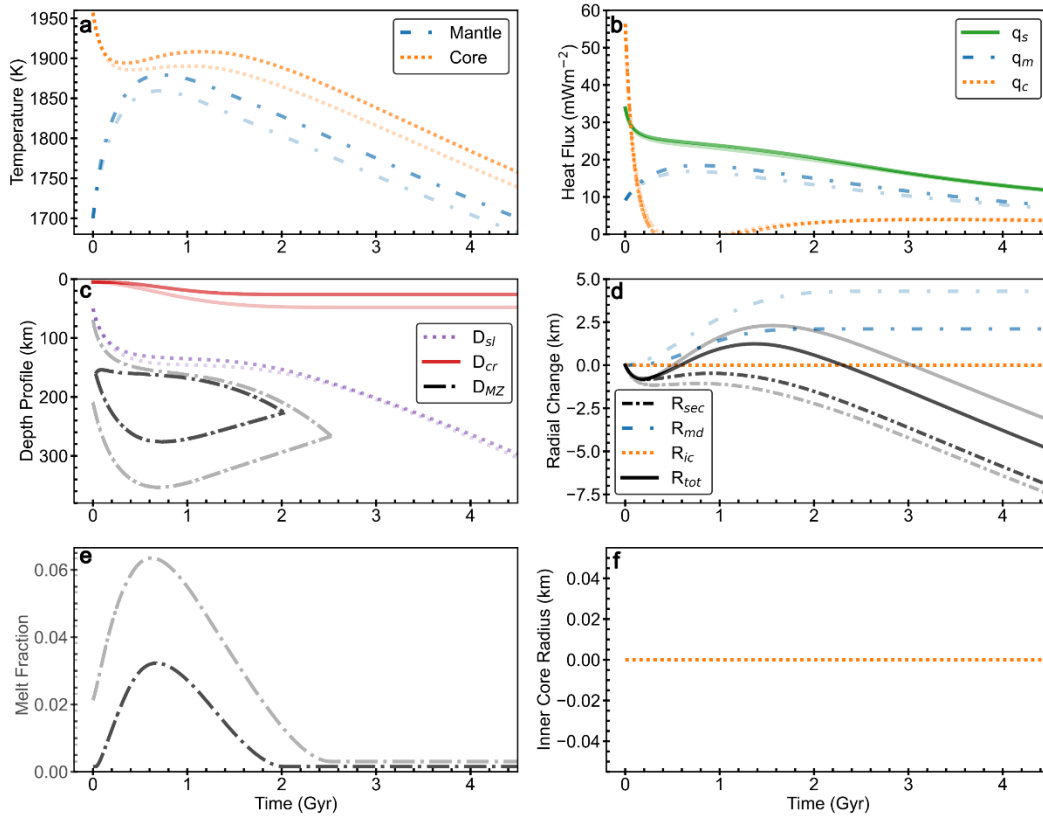


**Figure 2-4:** Model results using a Fe-free melt parameterization (*Namur et al., 2016*) and the same inputs as *Grott et al. (2011)* as a function of time. These results are overlaid on top of the peridotite melt parameterization (Figure 2-3; faded results) to highlight the difference in the model results. **(a)** Thermal profile of the core (orange dotted line) and the mantle (blue dash dot line). **(b)** Calculated heat fluxes: the core heat flux ( $q_c$  – dotted orange line), the mantle heat flux ( $q_m$  – blue dash dot line), and the surface heat flux ( $q_s$  – solid green line). **(c)** The silicate radial profile: the crustal depth ( $D_{cr}$  – solid red line), the stagnant lid depth ( $D_{sl}$  – dotted purple line), and the melt zone in the mantle ( $D_{mz}$  – black dash dot line). **(d)** Radial contraction profiles: due to inner core formation ( $R_{ic}$  – orange dotted line), due to mantle differentiation ( $R_{md}$  – blue dot dash line), due to secular cooling ( $R_{sec}$  – black dash-dot line), and total radial contraction of the planet ( $R_{tot}$  – solid black line). **(e)** Calculated volume averaged mantle melt fraction. **(f)** Calculated inner core radius.

### 2.3.3. Varying all three input parameters in a grid

To determine the effect of initial mantle temperature ( $T_{m,0}$ ), mantle reference viscosity ( $\eta_{ref}$ ), and initial core S concentration, we varied them systematically and compared the results to the constraints provided by the MESSENGER mission (Figures 2-5 through 2-10). The input values for these models are those in **Table 2-1** and **Table 2-2**, different from the above results.

### 2.3.3.1. Crustal thickness

The estimated present day crustal thickness from our results ranges from ~5 to ~75 km (**Figure 2-5**). Generally, the crustal thickness increases with increasing  $T_{m,0}$  and  $\eta_{ref}$  except for when the  $\eta_{ref}$  is  $10^{19}$  Pa s. Increasing initial core S content has a weak negative correlation in the amount of crust produced. The model results with the following input mantle conditions are:  $\eta_{ref} = 10^{19}$  Pa s at all temperatures and S contents;  $\eta_{ref} = 10^{20}$  Pa s at 1600 K and S contents <2.5 wt.%, 1700–1800 K and all S contents, and 1900 K and S contents >0.5 wt.%;  $\eta_{ref} = 10^{21}$  Pa s at 1700 K and all S contents; and  $\eta_{ref} = 10^{22}$  Pa s at 1800–1900 K and all S contents fall within the bounds of the estimated crustal thickness of 15–53 km (*Padovan et al.*, 2015; *Sori*, 2018). The  $\eta_{ref}$  and  $T_{m,0}$  are more significant drivers of the amount of present day crustal thickness than the initial core S content.

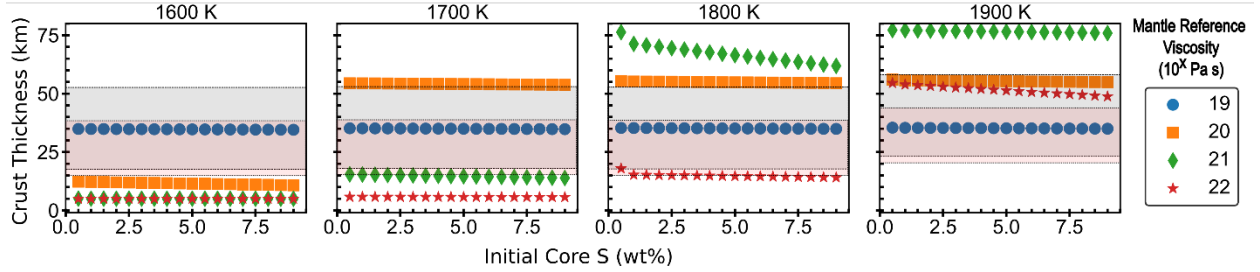


**Figure 2-5:** Calculated present day crustal thickness. The initial mantle temperature increases left to right from 1600 K to 1900 K, symbols correspond to different viscosity values: blue circles –  $10^{19}$  Pa s, orange squares –  $10^{20}$  Pa s, green diamonds –  $10^{21}$  Pa s, red stars –  $10^{22}$  Pa s. The red and gray bands indicate the bounds of crustal thickness estimates for present day Mercury: 15–53 km (*Padovan et al.*, 2015; *Sori*, 2018). Model results within the band are indicative of possible initial conditions for Mercury.

### 2.3.3.2. Cessation of mantle melting

The cessation time of mantle melting for all models considered ranges from 0 to ~2.8 Gyr after model start (**Figure 2-6**). Increasing the initial core S concentration causes melting to stop earlier in the planet’s history. Increasing  $T_{m,0}$  or  $\eta_{ref}$  causes the melting to continue longer throughout the planet’s history. A value of 0 for timing, indicates the model did not have any mantle melting. The models with the least change in melt cessation time at different  $T_{m,0}$  and initial core S concentrations were models run with a  $\eta_{ref}$  of  $10^{19}$  Pa s. The initial mantle temperature has a greater control on mantle melt cessation time than the initial core S concentration, and there is a moderate correlation between the higher  $\eta_{ref}$  and the cessation of mantle melt timing. As the trends for model results run at specific pairs of  $T_{m,0}$  and  $\eta_{ref}$  less than  $10^{22}$  Pa s do not change significantly with time, it can be stated that initial core S content has a small, if not negligible, correlation with

the cessation time of mantle melting. The model results which produce values fitting within the prescribed cessation of effusive volcanism by 3.7–3.5 Ga (Byrne *et al.*, 2016), are for model runs with  $\eta_{ref} = 10^{21}$  Pa s for all S contents and  $T_{m,0} = 1600$  K. Models that produce melt after this time are:  $\eta_{ref} = 10^{19}$ – $10^{21}$  Pa s for all S contents and  $T_{m,0}$ s, and  $\eta_{ref} = 10^{22}$  Pa s for all S contents and  $T_{m,0} > 1600$  K.

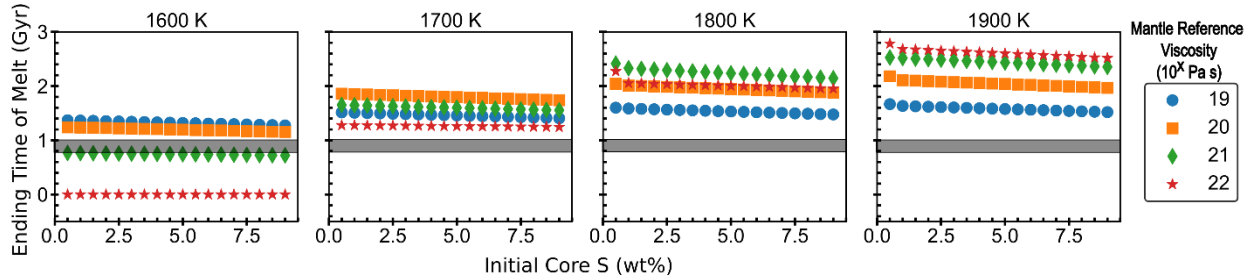


**Figure 2-6:** Calculated time of mantle melt cessation. The initial mantle temperature increases left to right from 1600 K to 1900 K, symbols correspond to different viscosity values as in Figure 2-5. The gray band represents the timing constraint of cessation of effusive volcanism by 3.7–3.5 Ga (Byrne *et al.*, 2016). Model results that plot at or above the band are relevant for present day Mercury.

### 2.3.3.3. Inner core radius

The calculated present day inner core radii span the entire range possible, from completely solid to completely liquid (**Figure 2-7**). Generally, as the initial core S concentration increases, the inner core radius decreases for all  $\eta_{ref} > 10^{19}$  Pa s. As  $\eta_{ref}$  increases, the inner core radius starts to decrease at smaller initial core S concentrations. Increasing  $T_{m,0}$  has no effect on the inner core radius until the  $\eta_{ref}$  is set to  $10^{22}$  Pa s. The models that yielded results which fall within the range of the maximum present day Mercury inner core radius constraint of  $1325 \pm 250$  km (Breuer *et al.*, 2015; Dumberry and Rivoldini, 2015) are:  $\eta_{ref} = 10^{20}$  Pa s for initial core S concentrations  $> 7$  wt.%,  $\eta_{ref} = 10^{21}$  Pa s for initial core S concentrations  $> 6$  wt.%, and  $\eta_{ref} = 10^{22}$  Pa s for initial core S concentrations  $> 5.5$  wt.% for low  $T_{m,0}$ , and  $> 3.5$  wt.% for high  $T_{m,0}$ . There is a clear correlation with inner core size and  $\eta_{ref}$ , and a weak correlation between  $T_{m,0}$  and inner core sizes.

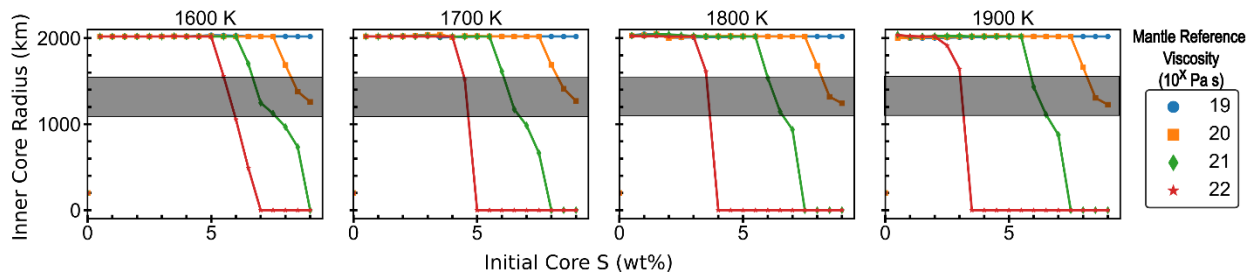


**Figure 2-7:** Calculated present day inner core radii. The initial mantle temperature increases left to right from 1600 K to 1900 K, symbols correspond to different viscosity values as in Figure 2-5.

The gray band indicates the upper limits on the present day inner core of radius:  $1325 \pm 250$  km (Breuer *et al.*, 2015; Dumberry and Rivoldini, 2015). Model values that plot within or under the band indicate possible conditions experienced by Mercury.

#### 2.3.3.4.Radial contraction

The calculated total radial contraction, with contributions from secular cooling, inner core formation, and crust formation ranges from -5 to -25 km (**Figure 2-8**). Increasing the initial core S concentration or  $T_{m,0}$ , increases the total amount of radial contraction. Increasing  $\eta_{ref}$  at a constant temperature, the total radial contraction decreases. Both  $T_{m,0}$  and  $\eta_{ref}$  influence the total radial contraction value of Mercury, with the initial amount of S in the core having a weaker effect. When the model results were compared to present day Mercury contraction estimates of 2–7 km (Byrne *et al.*, 2014; Claeys and Morbidelli, 2015; Watters, 2021), only three model runs fit within the total contraction constraint:  $\eta_{ref} = 10^{21}$  Pa s and at 1600 K, and  $\eta_{ref} = 10^{22}$  Pa s for 1600–1700 K, for all initial core S concentrations.

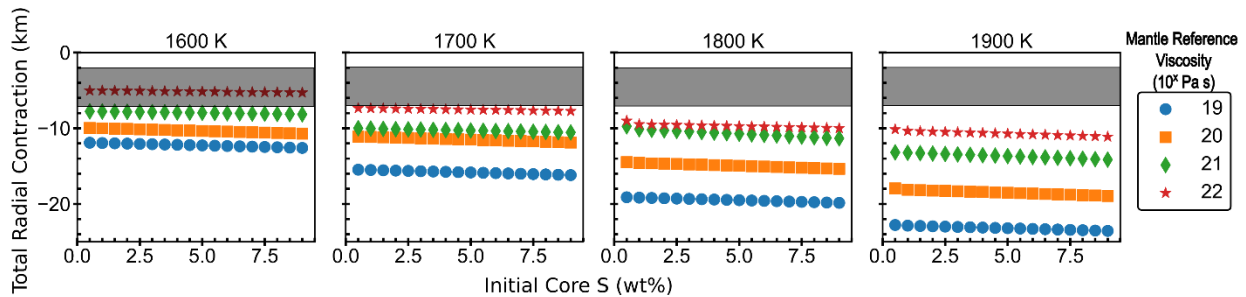


**Figure 2-8:** Present day total radial contraction. The initial mantle temperature increases left to right from 1600 K to 1900 K, symbols correspond to viscosity values as in Figure 2-5. The gray band represents the bounds on the total radial contraction estimates of 2–7 km (Byrne *et al.*, 2014; Claeys and Morbidelli, 2015; Watters, 2021). Model results plotting within that band are relevant for present day Mercury.

#### 2.3.3.5.Planetary mass

The present day calculated mass values range from  $\sim 3.8 \times 10^{23}$  to  $3.3 \times 10^{23}$  kg (**Figure 2-9**). Increasing the initial core S concentration causes the total mass of present day Mercury to decrease. Generally, increasing  $T_{m,0}$  and  $\eta_{ref}$  does not cause a notable change in the present day mass of Mercury. The initial amount of S in the core is a major control of the mass of the planet. All model runs with  $< 8.5$  wt.% S produce mass values greater than the mass of Mercury of  $3.301110 \pm 0.00015 \times 10^{23}$  kg (Margot *et al.*, 2018), due model limitations.

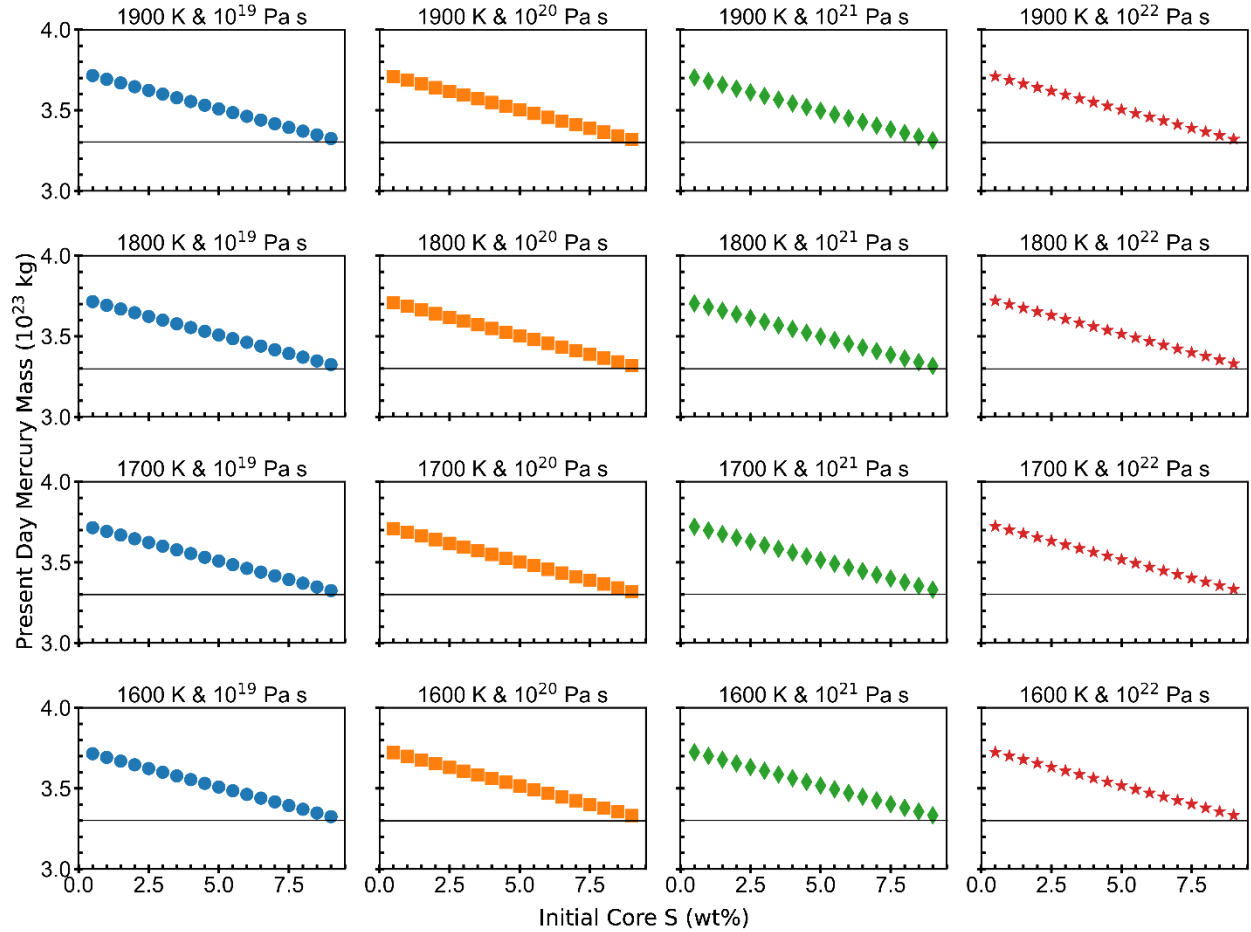


**Figure 2-9:** The calculated present day Mercury mass values. The mantle viscosity values increase from left to right from  $10^{19}$  Pa s to  $10^{22}$  Pa s, and initial mantle temperature decreases from top to bottom from 1900 K to 1600 K. The black line indicates the mass of Mercury at  $3.3 \times 10^{23}$  kg (*Margot et al.*, 2018). Successful models plot on the black line.

#### 2.3.3.6. Moment of Inertia

The calculated present day polar Mercury MOI factor ranged from 0.336 to 0.355 (**Figure 2-10**). For all  $T_{m,0}$  and  $\eta_{ref}$  values tested, the polar MOI factor increases with increasing initial core S content. All model results fit within the interval of acceptable MOI factors for present day Mercury of  $0.346 \pm 0.009$  (*Margot et al.*, 2012), indicating neither  $T_{m,0}$  nor  $\eta_{ref}$  influence the radial distribution of mass within the planet.

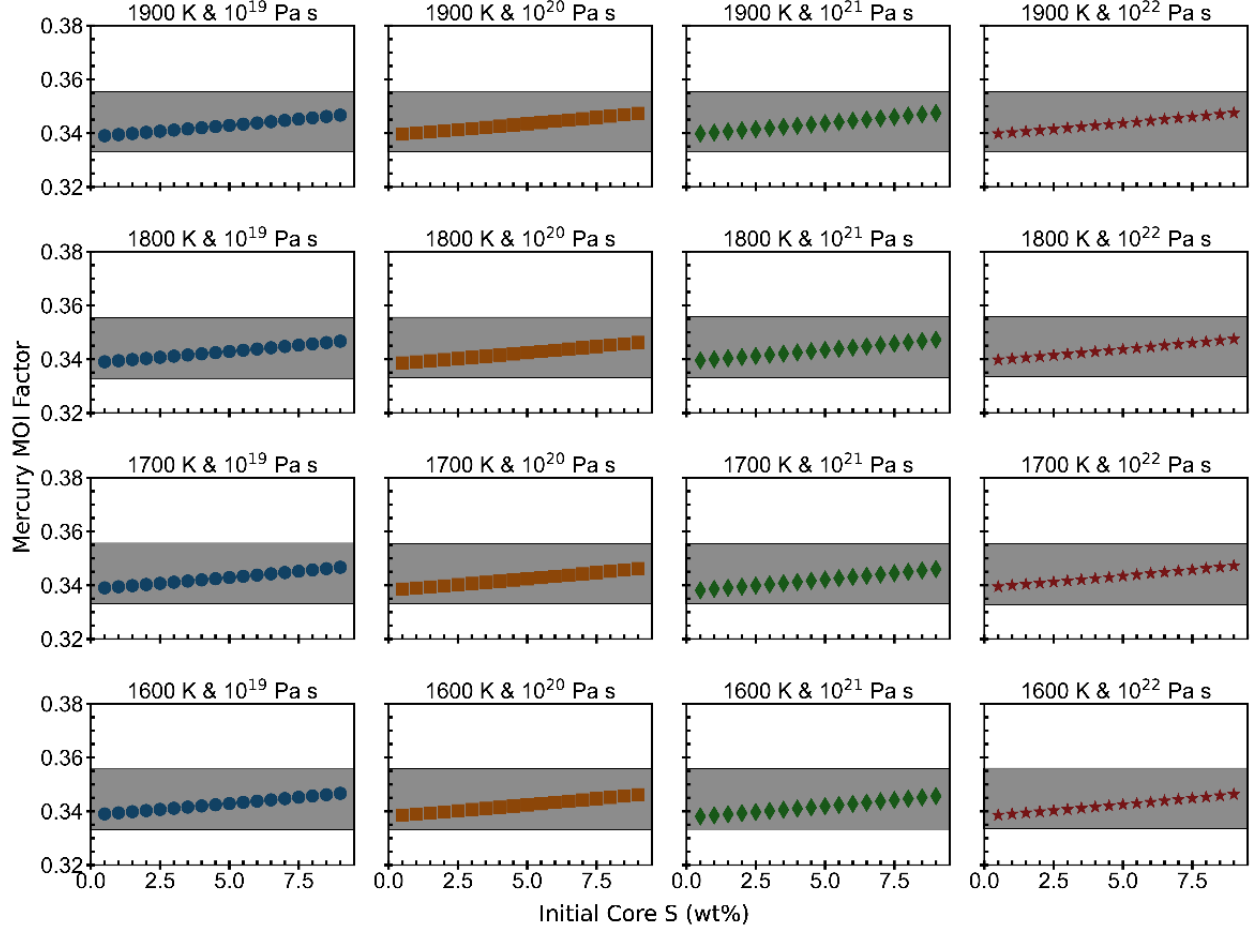


**Figure 2-10:** The calculated present day Mercury polar MOI factor. The mantle viscosity values increase from left to right from  $10^{19}$  Pa s to  $10^{22}$  Pa s, and initial mantle temperature decreases from top to bottom from 1900 K to 1600 K. The gray band indicates the range of Mercury’s MOI factor  $0.346 \pm 0.009$  (Margot *et al.*, 2012). Model values plotting within the band match Mercury.

### 2.3.3.7. Results summary

Changing the initial S concentrations has significant effects on the present day inner core radius and mass of the planet. Initial core S concentration has a small effect on the amount of crust produced at sufficiently high  $T_{m,0}$  and  $\eta_{ref}$ , the timing of melt cessation within the mantle, and the total radial contraction of the planet. Varying initial core S concentrations does not affect the present day polar MOI factor of the planet. Model results that fall within the estimated Mercury parameters are those with the starting conditions of  $\eta_{ref} = 10^{21} - 10^{22}$  Pa s, and an  $T_{m,0} = 1600$  K. These model runs fit five of the six constraints set for this study: the inner core size, the cessation time of partial melting, and the present day values of radial contraction, planetary mass, and MOI factor for Mercury. The constraint not fit by these models is the present day crust thickness. The other models run in this suite of tests fit less (or none) of the six Mercury-relevant constraints

described in Section 2.1.4. If we discount mantle mass and radial contraction, successful results occur when  $\eta_{ref} = 10^{20}$  Pa s,  $T_{m,0}$  are 1700, 1800, 1900 K, and initial core S concentrations are  $\geq 7$  wt.%. For  $\eta_{ref} = 10^{21}$  Pa s, successful results occur for an  $T_{m,0} = 1700$  K, and initial core S concentrations between 6–8.5 wt.%, and for  $\eta_{ref} = 10^{22}$  Pa s, successful results occur for an  $T_{m,0} = 1800$  K and initial core S concentrations 3.5 wt.%, and 1900 K and S = 2.5–3 wt.%.

## 2.4. Discussion

There were no combinations of initial core S, the  $T_{m,0}$ , and  $\eta_{ref}$  that satisfy all the present day Mercury parameters. However, the model does not account for all the factors that influenced Mercury’s evolution. For instance, this model does not account for a compositionally stratified core in the liquid outer core as in *Knibbe and van Westrenen (2015)*. Omitting this characteristic of Mercury’s thermochemical evolution lessened the computational costs but could be the cause of non-overlap of initial conditions that fit the present day Mercury constraints. Another reason there were not model results that fit within all the present day Mercury-relevant constraints is due to the way the constraints were incorporated in the model. For example, the timing of the deposition of the NSP (~1 Gyr after formation) was assumed to be the end of all volcanism on Mercury. However, recent studies have suggested that while Mercury’s effusive volcanism did terminate around that timeframe, Mercury experienced regional volcanism after that timeframe, indicating some form of partial melt was still forming within Mercury’s mantle. The amount of partial melt generated after 3.5 Ga would be significantly less than the amount generated within the first billion years after Mercury’s formation, which is consistent with the shape of the melt zone (Figure 2-4). Other potential reasons why the model results do not align with all the Mercury-relevant constraints derived from MESSENGER are discussed in the next sections.

### 2.4.1. Comparing the peridotite and Fe-free mantle melt parameterizations

The differences between the representative model run with the peridotite (**Figure 2-3**) and Fe-free (**Figure 2-4**) melt parameterization highlight the significance of using an appropriate mantle composition. The model run with the Fe-free melt parameterization has a higher mantle heat flux, causing a greater present day mantle and core temperature. As the planet cools, more heat is transferred from the mantle to the surface in the Fe-free melt parameterization compared to the peridotite melt parameterization, indicating that the Fe-free melt parameterization is more efficient at conducting heat out of the mantle. This also supports the difference in the amount and

cessation time of the partial melt that is generated in the mantle (**Figure 2-4c,e**). Less partial melt forming within the mantle means that less crust can form in the Fe-free melt parameterization model and so radial contraction due to mantle differentiation is less for the Fe-free melt parameterization than the peridotite melt parameterization. As mentioned above, using the Fe-free melt parameterization yielded a greater radial contraction due to secular cooling estimate for present day Mercury. This is also supported by the more efficient transfer of heat that occurred in the Fe-free melt parameterization model than in the peridotite melt parameterization model.

#### 2.4.2. Comparing the model results with present day Mercury

When the initial core S concentration was varied over 16 different  $T_{m,0}$  and  $\eta_{ref}$  values, it was clear that the initial core S concentration influences the size of the inner core, which effects the total radial contraction, mass, and MOI factor of present day Mercury. These trends are consistent with the fact that as more S is added to the core, the melt curve of the Fe+S core decreases (see the equation from *Rivoldini et al., 2011*), inhibiting the growth of the solid inner core in the model. For simplicity, we do not model core convection. With the onset of core crystallization, the liquid portion remains liquid longer as S is enriched, the heat in the core is not as efficiently removed from the core, causing the core to remain hotter and less heat gets transferred to the mantle. The more liquid the core is, the less the core mass is, leading to an overall lighter planet and a greater MOI factor which is seen in the model results. Even though the initial core S concentration was varied in all cases,  $T_{m,0}$  and  $\eta_{ref}$  have a stronger effect on the crustal thickness, the cessation of partial melt generation, and the total radial contraction of present day Mercury. This is consistent with the basic principles of petrology and geodynamics where the mineral composition of the mantle strongly affects how the mantle melts. The  $T_{m,0}$  has a stronger effect on the partial melt generation at higher  $\eta_{ref}$ . It is known that mantle viscosity, which is influenced by  $\eta_{ref}$  and  $T_{m,0}$  in this model, is a primary driver for mantle partial melt generation and duration (**Figure 2-6**).

Variations in  $\eta_{ref}$  are a main driver for the crustal thickness, the inner core radius, the cessation timing of mantle partial melt generation, and the present day total radial contraction of Mercury. Melt cessation timing is not significantly affected by varying the initial core S concentration or when  $\eta_{ref} = 10^{19}$ – $10^{20}$  Pa s, but does slightly change for model runs with  $\eta_{ref} = 10^{21}$  Pa s at 1800 and 1900 K. At these conditions, the core is completely crystallized, causing the mantle to cool faster than if the core had more liquid and was hotter. This finding is consistent

with the mantle viscosity affecting the amount and timing of partial melt generated in the mantle, and the vigor of mantle convection. As convection and conduction are the primary methods of heat transfer within a planetary mantle, mantle viscosity also indirectly controls how much heat flows through the mantle and the transfer of heat from the core to the surface of the planet. The greater the mantle's viscosity, the slower the mantle convection becomes, causing the mantle to retain more heat and be an insulating layer above the core. As such, less mantle melt can form in the mantle, which indicates that less crust can form when  $\eta_{ref}$  is higher. This leads to less radial contraction due to mantle differentiation. Because the mantle is more insulating in this context, the mantle retains more heat causing the core to retain more heat as well, which affects the maximum size of the inner core.

The change in the amount of melt generated within the mantle affects how much crust can be accumulated in each model. Thus, this also affects the radial expansion caused by the mantle differentiation. Less crust generated in the model run leads to less radial expansion, causing more radial contraction for the model. Varying the initial core S content does not have a significant impact on the present day total contraction amount of Mercury, as it only affects change in inner core radius. This is a smaller radial change contribution compared to the secular cooling radial change contribution, which is consistent with the findings in *Grott et al.* (2011). Increasing  $\eta_{ref}$  decreases the amount of radial contraction, because the contraction due to secular cooling decreases. The hotter the mantle (and thus the planet), the less the planet cools over time. However, only a few models fit within the estimated planetary contraction bounds from the MESSENGER mission. The calculated total contraction of the planet for most of the runs was greater than the estimated upper bounds of the contraction limit. This mismatch could be due to multiple factors. A potential factor could be caused by the low estimate of the change in mantle volume upon mantle differentiation. While this was calculated based on a ratio between intrusive and extrusive volcanism on Mercury, the ratio was based on an assumption that the crust of the planet is ~10 vol.% of the total volume of silicate materials in the planet (*Padovan et al.*, 2015; *Padovan et al.*, 2017). Additionally, this was based on a depleted mantle density of 3150 kg/m<sup>3</sup>, derived from the assumption that mantle is mostly composed of silicates with some Fe sulfides (*Lark et al.*, 2022; *Vander Kaaden and McCubbin*, 2015). Mercury's mantle composition may have more Mg-Ca sulfides (*Dasgupta et al.*, 2022), and adding more Mg-Ca sulfides to Mercury's mantle should

cause the density of the mantle to decrease (*Vander Kaaden and McCubbin, 2015*), and therefore, the depleted mantle density should decrease as well, affecting the present day Mercury mass value.

All the calculated planetary masses were greater than the estimated mass for Mercury derived from the MESSENGER mission. The model calculates mantle densities as a constant value, instead of depth-dependent densities. The crust was also assumed to have a constant density, but the crust has been found to have lateral densities which affect the crustal thickness (*Beuthe et al., 2020*). While these layers are relatively thin compared to Mercury's core, the lateral density variations in the crust and the depth-dependent densities in the mantle would influence the present day mass calculation for the planet. Additionally, while the core composition for this model was assumed to be Fe+S, studies have proposed that the core of Mercury is potentially composed of some combination of Fe-S-Si, and possibly C (*Chabot et al., 2014; Edmund et al., 2022; Knibbe and van Westrenen, 2015; Vander Kaaden et al., 2020*). These studies indicated that is potentially more Si in the core than S; thus, the core will have a different composition and a lighter density than what is studied here (see Section 2.1.1). Overall, due to simplifications made during the study, the Mercury mass results are currently overestimated. To fix this, the considerations above would have to be added to the model, adding to the model complexity.

Interestingly, the calculated polar MOI factor for Mercury from all models fit within the bounds predicted from the MESSENGER data. This indicates that while the mass of the planet is overestimated, the radial distribution of the mass in these models is appropriate for Mercury. As found in the results,  $T_{m,0}$  and  $\eta_{ref}$  used in each model do not have a strong control on the calculated MOI values. The initial core S concentration influenced the calculated MOI factor, as the concentration of S in the core at any point during the model run influenced how big the inner core can become.

#### 2.4.3. Inner core calculations

The modified inner core calculation, which accounted for the inner core crystallizing for the top-down (similar to Ganymede) and from the bottom-up (similar to Earth) or some combination of the two approaches, did not change the expected inner core radii values significantly compared to the assumption that Mercury's solid inner core only formed from the bottom-up. However, it more accurately reflects the geochemistry occurring within the core (with the assumed core composition), as it accounts for the changing densities for the inner and outer core as the solid inner core forms (because S preferentially remains in the liquid rather than in the

solid as discussed above), and for the change in the central pressure of Mercury, as layers of solid Fe (top-down crystallization method) or a sphere of solid Fe (bottom up crystallization method) nucleate and grow within the inner core, causing a different mass distribution within the core. In many of the runs, the combination of both core formation methods was observed, as the inner core melt curve changed slope with the growth of the solid inner core. When this happened, the volume of Fe in the snow zones was determined, and then was converted to a mass of solid Fe. Because masses are additive, the solid Fe mass was added to the solid inner core (formed through the bottom-up core crystallization pathway) to obtain a total inner core radius at the current timestep of the model. The step-wise slope in the inner core melt curve led to multiple intersections within the inner core formation algorithm; but the final inner core radial value (after the solid Fe in the Fe snow zones was brought to the core center or the top of the inner core) was only accepted if the calculated values were found to be stable via a convergence test.

#### *2.4.4. Model Limitations and future work suggestions*

One of the major limitations in the model is the simplistic approach for the formation of the snow zone within Mercury's core. Current research indicates that when top-down crystallization occurs, multiple snow zones can occur as is suggested by *Hauck et al.* (2006) for Ganymede, and (*Dumberry and Rivoldini, 2015*) for Mercury. An assumption in our model is that all the snow zone region crystallizes into solid Fe and is brought down to the top of the inner core (if present) or the center of the planet (if no inner core is present). However, not all the Fe in the snow zones crystallizes and sinks as the model assumes. The snow zones only crystallize some of the solid Fe contained within them, not all (*Dumberry and Rivoldini, 2015; Hauck et al., 2006; Rückriemen et al., 2018; Vilim et al., 2010*), and so the model overestimates the amount of solid Fe that would crystallize and sink within the core, leading to a chemical gradient within the core that needs to be tracked. This leads to a larger estimate of the present day inner core in this study than other studies. While accounting for the chemical gradient in the model is out of the scope of this study, future studies will need to account for the chemical gradient to ensure that the inner core is calculated as precisely as possible. Additionally, the model does not account for the energy change produced by the sinking of solid Fe from the snow zone to the inner core (or the center of the planet) for calculation simplicity, as in (*Rückriemen et al., 2015*). Any form of solid Fe that would form within the Fe snow zones in Mercury were instantaneously brought to the center of the core. As such, the energy within the core is an overestimate; because dropping the solid

particles out of the liquid phase would lead to a decrease in the potential energy of the system because of gravitational settling (*Turcotte and Schubert, 2002*). Adding in the change in core energy due to dissipation would increase computing time and power and is out of scope for this project. Future work would need to incorporate this consideration in their models to appropriately account for Mercury's energy balance.

Another limitation of the model is that the change in the inner core radius as a function of the CMB temperature is only calculated based on the CMB temperature and the thickness of the crust on Mercury. This derivative also depends on the range of S concentrations plausible for Mercury's core; however, this was omitted due to the computational costs and time. The range of crustal thicknesses was used due to the limited role it has in the inner calculation. This allows the temperature range over which the derivative is calculated to be much denser and leads to a better inner core derivative determination than used by *Grott et al. (2011)* via personal communication. The inner core is calculated within each iteration of the model (every time step), but the grid derivative is only calculated at the beginning of each run. While the derivative is only calculated once, the resulting derivative is interpolated using a multi-dimensional interpolation over a grid of potential core temperature and crust radius at each time step. Adding in the dependence of the inner core calculation on the core S concentration into this multi-dimensional interpolation would lead to a more complex inner core derivative with respect to CMB temperature calculation, and a longer multi-dimensional interpolation within each model run. Because this model does not include the current S concentration at each time-step in the model, the derivative of the inner core with respect to the CMB temperature is not as accurate as it could be. Though the model does not account for this due to simplicity and ease of computational costs, the method used to calculate the inner core derivative with respect to the CMB temperature is more accurate than only performing a finite difference of the inner core just based on the CMB temperature as done in *Grott et al. (2011)*.

For the mantle, the model assumes a compositionally homogenous lherzolite source, following the findings of (*Namur et al., 2016*). Geochemically, it has been shown that Mercury's mantle is heterogenous with two different source regions predicted for the surface lavas (*Charlier et al., 2013; Mouser and Dygert, 2023; Namur et al., 2016; Vander Kaaden et al., 2017*). As shown in previous geochemical work, these source lavas may be a result of a compositionally layered mantle. The mantle heterogeneity would affect the melting behavior of the mantle, the crust

production, and the heat flux through the mantle by its effect on the mantle temperature. As such, it is possible the model is not completely geochemically accurate. Future studies should account for the heterogeneity of Mercury's mantle by including the thermodynamic relationships of each mantle mineral phase that will affect the amount and composition of the partial melt within the mantle, which has implications for the overall heat retained and transferred in the mantle, leading to an effect on the overall heat flux of Mercury itself.

## 2.5. Conclusions

This study used a modified 1D thermochemical model to explore how Mercury evolved over 4.5 billion years. We used a mantle melt parameterization that reflects the Fe poor nature of Mercury, and calculated the inner core nucleation and growth using two different approaches: a top-down approach, a bottom-up approach, or some combination of the two. The model varied the initial core sulfur content over a grid of initial mantle temperatures and mantle reference viscosities thought to be appropriate for Mercury's evolution. All results of the model were compared to Mercury-relevant constraints found from the MESSENGER mission: crustal thickness, inner core size, partial melt cessation time, total radial contraction, planetary mass, and polar MOI factor.

There were only two models that fit most (but not all) of the constraints of Mercury: the model with the initial mantle temperature of 1600 K and a mantle reference viscosity of  $10^{21}$  Pa s, and the model with the initial mantle temperature of 1600 K and a mantle reference viscosity of  $10^{22}$  Pa s. The rest of the models run in this study fit less, and in some cases: none, of the constraints. The main limitations of the model are the simplified composition of the core and mantle, and the Fe snow calculations were over simplified. Future work for this study would entail adding more complexity to the inner core algorithm to fully account for all the compositional and energy gradients that would occur as the inner core forms, adding the compositional effects of additional light elements in the core to determine how the core composition changes as an inner core grows. Finally, another addition to the model would be to account for the proposed heterogeneity in Mercury's mantle using a solidus that accounts for both the lherzolite and the harzburgite sources that are proposed to be in Mercury's mantle.

More information will be collected from the ESA/JAXA BepiColombo mission which will provide much needed insights into how Mercury was able to form and evolve close to the Sun, the surface processes that Mercury has experienced over the past 4.5 billion years, and the geochemical

composition and internal structure of Mercury (*Benkhoff et al.*, 2010). Utilizing the data from BepiColombo in conjunction with the data from the MESSENGER mission will lead to improved models about Mercury's thermochemical evolution, and the evolutionary processes experienced by Mercury including volcanism, tectonics, and impacts.

### 3. Conclusions of Project

This work investigates the planetary evolution of Mercury to determine potential initial conditions experienced by Mercury right after formation. These conditions dictate what processes can occur within the planet as it evolves, which affects the transfer of heat from the planet's center outward to the surface, where it dissipates into space. As highlighted here, Mercury is significantly different from Earth, so multiple methods, assumptions, and made for Earth's evolution do not apply here (i.e., the peridotite mantle solidus (*Grott et al.*, 2011; *Hauck et al.*, 2013; *Michel et al.*, 2013; *Tosi et al.*, 2013; *Tosi et al.*, 2015), a purely bottom-up inner core crystallization composition (*Grott et al.*, 2011; *Hauck et al.*, 2004; *Michel et al.*, 2013; *Tosi et al.*, 2013), and the stagnant lid (*Tosi and Padovan*, 2021)). Due to Mercury's small size but large core and relatively thin mantle, the radial profile of Mercury is significantly different from the radial profile seen on Earth. Thus, the heat transfer processes that occur on Mercury are different than the heat transfer processes occurring on Earth, indicating Mercury is a natural laboratory for non-Earth like heat transfers. However, not much is known about heat-transfer processes that occur in non-Earth like environments.

The heat transfer within the planet controls the evolutionary processes that occur in the planet's interior. This work highlights the potential evolutionary paths for Mercury, including partial melt generation, inner core crystallization, and planetary contraction. While partial melt generation and inner core crystallization are also inferred for other terrestrial planets like Mars and Earth, Mercury's partial melt generation occurs in a much more reduced and thinner environment than seen on Mars or Earth.

## 4. References

- Anzures, B. A., Parman, S. W., Milliken, R. E., Namur, O., Cartier, C. and Wang, S. C. (2020) Effect of sulfur speciation on chemical and physical properties of very reduced mercurian melts. *Geochimica et Cosmochimica Acta*, **286**, 1-18. doi: 10.1016/j.gca.2020.07.024
- Benkhoff, J., van Casteren, J., Hayakawa, H., Fujimoto, M., Laakso, H., Novara, M., Ferri, P., Middleton, H. R. and Ziethe, R. (2010) BepiColombo-Comprehensive exploration of Mercury: Mission overview and science goals. *Planetary and Space Science*, **58**, 2-20. doi: 10.1016/j.pss.2009.09.020
- Berrada, M., Secco, R. A. and Yong, W. (2021) Adiabatic heat flow in Mercury's core from electrical resistivity measurements of liquid Fe-8.5 wt.% Si to 24 GPa. *Earth and Planetary Science Letters*, **568**, 117053. doi: 10.1016/j.epsl.2021.117053
- Beuthe, M., Charlier, B., Namur, O., Rivoldini, A. and Van Hoolst, T. (2020) Mercury's crustal thickness correlates with lateral variations in mantle melt production. *Geophysical Research Letters*, **47**, e2020GL087261. doi: 10.1029/2020GL087261
- Breuer, D., Rueckriemen, T. and Spohn, T. (2015) Iron snow, crystal floats, and inner core growth: Modes of core solidification and implications for dynamos in terrestrial planets and moons. *Progress in Earth and Planetary Science*, **2**, 39. doi: 10.1186/s40645-015-0069-y
- Byrne, P. K., Klimczak, C., Sengör, A. M. C., Solomon, S. C., Watters, T. R. and Hauck, S. A. (2014) Mercury's global contraction much greater than earlier estimates. *Nature Geoscience*, **7**, 301-307. doi: 10.1038/ngeo2097
- Byrne, P. K., Ostrach, L. R., Fassett, C. I., Chapman, C. R., Denevi, B. W., Evans, A. J. and Solomon, S. C. (2016) Widespread effusive volcanism on Mercury likely ended by about 3.5 Ga. *Geophysical Research Letters*, **43**, 7408-7416. doi: 10.1002/2016GL069412
- Chabot, N. L., Wollack, E. A., Klima, R. L. and Minitti, M. E. (2014) Experimental constraints on Mercury's core composition. *Earth and Planetary Science Letters*, **390**, 199-208. doi: 10.1016/j.epsl.2014.01.004
- Charlier, B., Grove, T. L. and Zuber, M. T. (2013) Phase equilibria of ultramafic compositions on Mercury and the origin of the compositional dichotomy. *Earth and Planetary Science Letters*, **363**, 50-60. doi: 10.1016/j.epsl.2012.12.021
- Charlier, B. and Namur, O. (2019) The origin and differentiation of planet Mercury. *Elements*, **15**, 9-14. doi: 10.2138/gselements.15.1.9
- Choblet, G. and Sotin, C. (2000) 3D thermal convection with variable viscosity: Can transient cooling be described by a quasi-static scaling law? *Physics of the Earth and Planetary Interiors*, **119**, 321-336. doi: 10.1016/S0031-9201(00)00136-9
- Claeys, P. and Morbidelli, A. (2015) Late heavy bombardment, in: *Encyclopedia of Astrobiology*, Gargaud, M., Irvine, W. M., Amils, R., Cleaves, H. J., Pinti, D. L., Quintanilla, J. C., Rouan, D., Spohn, T., Tirard, S., Viso, M. (Eds.), pp. 1365-1369.
- Dasgupta, R., Chowdhury, P., Eguchi, J., Sun, C. and Saha, S. (2022) Volatile-bearing partial melts in the lithospheric and sub-lithospheric mantle on Earth and other rocky planets, in: *Geological Melts*, **87**, pp. 575-606.
- Davaille, A. and Jaupart, C. (1993) Transient high-Rayleigh-number thermal-convection with large viscosity variations. *Journal of Fluid Mechanics*, **253**, 141-166. doi: 10.1017/S0022112093001740
- Dumberry, M. and Rivoldini, A. (2015) Mercury's inner core size and core-crystallization regime. *Icarus*, **248**, 254-268. doi: 10.1016/j.icarus.2014.10.038

- Edmund, E., Morard, G., Baron, M. A., Rivoldini, A., Yokoo, S., Boccato, S., Hirose, K., Pakhomova, A. and Antonangeli, D. (2022) The Fe-FeSi phase diagram at Mercury's core conditions. *Nature Communications*, **13**, 387. doi: 10.1038/s41467-022-27991-9
- European Space Agency. 2024. Three reasons why we know so little about Mercury. [https://www.esa.int/Science\\_Exploration/Space\\_Science/BepiColombo/Three\\_reasons\\_why\\_we\\_know\\_so\\_little\\_about\\_Mercury](https://www.esa.int/Science_Exploration/Space_Science/BepiColombo/Three_reasons_why_we_know_so_little_about_Mercury)
- Evans, L. G., Peplowski, P. N., Rhodes, E. A., Lawrence, D. J., McCoy, T. J., Nittler, L. R., Solomon, S. C., Sprague, A. L., Stockstill-Cahill, K. R., Starr, R. D., Weider, S. Z., Boynton, W. V., Hamara, D. K. and Goldsten, J. O. (2012) Major element abundances on the surface of Mercury: Results from the MESSENGER Gamma-Ray Spectrometer. *Journal of Geophysical Research: Planets*, **117**, E00107. doi: 10.1029/2012je004178
- Gale, A., Dalton, C. A., Langmuir, C. H., Su, Y. J. and Schilling, J. G. (2013) The mean composition of ocean ridge basalts. *Geochemistry Geophysics Geosystems*, **14**, 489-518. doi: 10.1029/2012gc004334
- Genova, A., Goossens, S., Mazarico, E., Lemoine, F. G., Neumann, G. A., Kuang, W., Sabaka, T. J., Hauck, S. A., Smith, D. E., Solomon, S. C. and Zuber, M. T. (2019) Geodetic evidence that Mercury has a solid inner core. *Geophysical Research Letters*, **46**, 3625-3633. doi: 10.1029/2018GL081135
- Goossens, S., Genova, A., James, P. B. and Mazarico, E. (2022) Estimation of crust and lithosphere properties for Mercury from high resolution gravity and topography. *The Planetary Science Journal*, **3**
- Grasset, O. and Parmentier, E. M. (1998) Thermal convection in a volumetrically heated, infinite Prandtl number fluid with strongly temperature-dependent viscosity: Implications for planetary thermal evolution. *Journal of Geophysical Research: Solid Earth*, **103**, 18171-18181. doi: 10.1029/98jb01492
- Grott, M., Breuer, D. and Laneuville, M. (2011) Thermo-chemical evolution and global contraction of Mercury. *Earth and Planetary Science Letters*, **307**, 135-146. doi: 10.1016/j.epsl.2011.04.040
- Grott, M. (2022) Personal communication.
- Guerrero, J. M., Lowman, J. P. and Tackley, P. J. (2021) Did the cessation of convection in Mercury's mantle allow for a dynamo supporting increase in heat loss from its core? *Earth and Planetary Science Letters*, **571**
- Hauck, S. A., Dombard, A. J., Phillips, R. J. and Solomon, S. C. (2004) Internal and tectonic evolution of Mercury. *Earth and Planetary Science Letters*, **222**, 713-728. doi: 10.1016/j.epsl.2004.03.037
- Hauck, S. A., Aurnou, J. M. and Dombard, A. J. (2006) Sulfur's impact on core evolution and magnetic field generation on Ganymede. *Journal of Geophysical Research: Planets*, **111**, E09008. doi: 10.1029/2005je002557
- Hauck, S. A., Margot, J. L., Solomon, S. C., Phillips, R. J., Johnson, C. L., Lemoine, F. G., Mazarico, E., McCoy, T. J., Padovan, S., Peale, S. J., Perry, M. E., Smith, D. E. and Zuber, M. T. (2013) The curious case of Mercury's internal structure. *Journal of Geophysical Research: Planets*, **118**, 1204-1220. doi: 10.1002/jgre.20091
- Hauck, S. A., Grott, M., Byrne, P. K., Denevi, B. W., Stanley, S. and McCoy, T. J. (2018) Mercury's global evolution, in: *Mercury: The View After MESSENGER*, Solomon, S. C., Nittler, L. R., Anderson, B. J. (Eds.), Ch. 19. Cambridge University Press, pp. 371-406.

- Head, J. W., Chapman, C. R., Strom, R. G., Fassett, C. I., Denevi, B. W., Blewett, D. T., Ernst, C. M., Watters, T. R., Solomon, S. C., Murchie, S. L., Prockter, L. M., Chabot, N. L., Gillis-Davis, J. J., Whitten, J. L., Goudge, T. A., Baker, D. M. H., Hurwitz, D. M., Ostrach, L. R., Xiao, Z., Merline, W. J., Kerber, L., Dickson, J. L., Oberrst, J., Byrne, P. K., Klimczak, C. and Nittler, L. R. (2011) Flood volcanism in the northern high latitudes of Mercury revealed by MESSENGER. *Science*, **333**, 1853-1856. doi: 10.1126/science.1211997
- Hemingway, D. J. and Driscoll, P. E. (2021) History and future of the martian dynamo and implications of a hypothetical solid inner core. *Journal of Geophysical Research: Planets*, **126**, e2020JE006663. doi: 10.1029/2020JE006663
- Hüttig, C., Tosi, N. and Moore, W. (2013) An improved formulation of the incompressible Navier-Stokes equations with variable viscosity. *Physics of the Earth and Planetary Interiors*, **220**. doi: 10.1029/2009JE003456
- Jing, Z. C., Wang, Y. B., Kono, Y., Yu, T., Sakamaki, T., Park, C., Rivers, M. L., Sutton, S. R. and Shen, G. Y. (2014) Sound velocity of Fe-S liquids at high pressure: Implications for the Moon's molten outer core. *Earth and Planetary Science Letters*, **396**, 78-87. doi: 10.1016/j.epsl.2014.04.015
- Karato, S. and Wu, P. (1993) Rheology of the upper mantle: A synthesis. *Science*, **260**, 771-8. doi: 10.1126/science.260.5109.771
- Katayama, I. (2021) Strength models of the terrestrial planets and implications for their lithospheric structure and evolution. *Progress in Earth and Planetary Science*, **8**. doi: 10.1186/s40645-020-00388-2
- Kelsey, C. H. (1965) Calculation of the C.I.P.W. Norm. *Mineralogical Magazine and Journal of the Mineralogical Society*, **34**, 276-282. doi: 10.1180/minmag.1965.034.268.23
- Knibbe, J. S. and van Westrenen, W. (2015) The interior configuration of planet Mercury constrained by moment of inertia and planetary contraction. *Journal of Geophysical Research: Planets*, 1904-1923
- Komabayashi, T. and Fei, Y. (2010) Internally consistent thermodynamic database for iron to the Earth's core conditions. *Journal of Geophysical Research: Solid Earth*, **115**, B03202. doi: 10.1029/2009jb006442
- Lark, L. H., Parman, S., Huber, C., Parmentier, E. M. and Head, J. W. (2022) Sulfides in Mercury's mantle: Implications for Mercury's interior as interpreted from moment of inertia. *Geophysical Research Letters*, **49**, e2021GL096713. doi: 10.1029/2021GL096713
- Li, J., Fei, Y., Mao, H. K., Hirose, K. and Shieh, S. R. (2001) Sulfur in the Earth's inner core. *Earth and Planetary Science Letters*, 509-514
- Mackwell, S. J. (1991) High temperature rheology of enstatite - Implications for creep in the mantle. *Geophysical Research Letters*, **18**, 2027-2030. doi: 10.1029/91gl02492
- Malavergne, V., Cordier, P., Righter, K., Brunet, F., Zanda, B., Addad, A., Smith, T., Bureau, H., Surblé, S., Raepsaet, C., Charon, E. and Hewins, R. H. (2014) How Mercury can be the most reduced terrestrial planet and still store iron in its mantle. *Earth and Planetary Science Letters*, **394**, 186-197. doi: 10.1016/j.epsl.2014.03.028
- Mallama, A. (2009) Characterization of terrestrial exoplanets based on the phase curves and albedos of Mercury, Venus and Mars. *Icarus*, **204**, 11-14. doi: 10.1016/j.icarus.2009.07.010
- Margot, J.-L., Hauck, S. A., Mazarico, E., Padovan, S. and Peale, S. J. (2018) Mercury's internal structure, in: *Mercury: The View After MESSENGER*, Solomon, S. C., Nittler, L. R., Anderson, B. J. (Eds.). Cambridge University Press, pp. 85-113.

- Margot, J. L., Peale, S. J., Solomon, S. C., Hauck, S. A., Ghigo, F. D., Jurgens, R. F., Yseboodt, M., Giorgini, J. D., Padovan, S. and Campbell, D. B. (2012) Mercury's moment of inertia from spin and gravity data. *Journal of Geophysical Research: Planets*, **117**, E00109. doi: 10.1029/2012je004161
- McCoy, T. J. and Nittler, L. R. (2014) Mercury, in: *Treatise on Geochemistry*, Holland, H. D., Turekian, K. K. (Eds.), Ch. 2.6, pp. 119-126.
- McCoy, T. J., Peplowski, P. N., McCubbin, F. M. and Weider, S. Z. (2018) The geochemical and mineralogical diversity of Mercury, in: *Mercury: The View After MESSENGER*, Solomon, S. C., Nittler, L. R., Anderson, B. J. (Eds.), Ch. 7. Cambridge University Press, pp. 176-190.
- Michel, N. C., Hauck, S. A., Solomon, S. C., Phillips, R. J., Roberts, J. H. and Zuber, M. T. (2013) Thermal evolution of Mercury as constrained by MESSENGER observations. *Journal of Geophysical Research: Planets*, **118**, 1033-1044. doi: 10.1002/jgre.20049
- Morschhauser, A., Grott, M. and Breuer, D. (2011) Crustal recycling, mantle dehydration, and the thermal evolution of Mars. *Icarus*, **212**, 541-558. doi: 10.1016/j.icarus.2010.12.028
- Mouser, M. D. and Dygert, N. (2023) On the potential for cumulate mantle overturn in Mercury. *Journal of Geophysical Research: Planets*, **128**, e2023JE007739. doi: 10.1029/2023JE007739
- Namur, O., Collinet, M., Charlier, B., Grove, T. L., Holtz, F. and McCammon, C. (2016) Melting processes and mantle sources of lavas on Mercury. *Earth and Planetary Science Letters*, **439**, 117-128. doi: 10.1016/j.epsl.2016.01.030
- National Academies of Sciences, E., and Medicine (2023) *Origins, Worlds, and Life: A Decadal Strategy for Planetary Science and Astrobiology 2023-2032*. The National Academies Press, Washington, DC.
- Ness, N. F., Behannon, K. W., Lepping, R. P. and Whang, Y. C. (1975) The magnetic field of Mercury. *Journal of Geophysical Research*, 2708-2716
- Ness, N. F., Behannon, K. W., Lepping, R. P. and Whang, Y. C. (1976) Observations of Mercury's magnetic field. *Icarus*, 479-488
- Nittler, L. R., Starr, R. D., Weider, S. Z., McCoy, T. J., Boynton, W. V., Ebel, D. S., Ernst, C. M., Evans, L. G., Goldsten, J. O., Hamara, D. K., Lawrence, D. J., McNutt, R. L., Schlemm, C. E., Solomon, S. C. and Sprague, A. L. (2011) The major element composition of Mercury's surface from MESSENGER X-ray spectrometry. *Science*, **333**, 1847-50. doi: 10.1126/science.1211567
- Nittler, L. R., Chabot, N. L., Grove, T. L. and Peplowski, P. N. (2018) The chemical composition of Mercury, in: *Mercury: The View After MESSENGER* Solomon, S. C., Nittler, L. R., Anderson, B. J. (Eds.). Cambridge University Press, pp. 30-51.
- O'Neill, C. O., Jellinek, A. M. and Lenardic, A. (2007) Conditions for the onset of plate tectonics on terrestrial planets and moons. *Earth and Planetary Science Letters*, 20-32
- Padovan, S., Wiczorek, M. A., Margot, J. L., Tosi, N. and Solomon, S. C. (2015) Thickness of the crust of Mercury from geoid-to-topography ratios. *Geophysical Research Letters*, **42**, 1029-1038. doi: 10.1002/2014gl062487
- Padovan, S., Tosi, N., Plesa, A. C. and Ruedas, T. (2017) Impact-induced changes in source depth and volume of magmatism on Mercury and their observational signatures. *Nature Communications*, **8**, 1945. doi: 10.1038/s41467-017-01692-0
- Peplowski, P. N., Lawrence, D. J., Rhodes, E. A., Sprague, A. L., McCoy, T. J., Denevi, B. W., Evans, L. G., Head, J. W., Nittler, L. R., Solomon, S. C., Stockstill-Cahill, K. R. and

- Weider, S. Z. (2012) Variations in the abundances of potassium and thorium on the surface of Mercury: Results from the MESSENGER Gamma-Ray Spectrometer. *Journal of Geophysical Research: Planets*, **117**. doi: 10.1029/2012JE004141
- Peplowski, P. N., Evans, L. G., Stockstill-Cahill, K. R., Lawrence, D. J., Goldsten, J. O., McCoy, T. J., Nittler, L. R., Solomon, S. C., Sprague, A. L., Starr, R. D. and Weider, S. Z. (2014) Enhanced sodium abundance in Mercury's north polar region revealed by the MESSENGER Gamma-Ray Spectrometer. *Icarus*, **228**, 86-95. doi: 10.1016/j.icarus.2013.09.007
- Perry, M. E., Kahan, D. S., Barnouin, O. S., Ernst, C. M., Solomon, S. C., Zuber, M. T., Smith, D. E., Phillips, R. J., Srinivasan, D. K., Oberst, J. and Asmar, S. W. (2011) Measurement of the radius of Mercury by radio occultation during the MESSENGER flybys. *Planetary and Space Science*, **59**, 1925-1931. doi: 10.1016/j.pss.2011.07.022
- Peterson, G. A., Johnson, C. L. and Jellinek, A. M. (2021) Thermal evolution of Mercury with a volcanic heat-pipe flux: Reconciling early volcanism, tectonism, and magnetism. *Science Advances*, **7**, eabh2482. doi: 10.1126/sciadv.abh2482
- Pommier, A. (2018) Influence of sulfur on the electrical resistivity of a crystallizing core in small terrestrial bodies. *Earth and Planetary Science Letters*, **496**, 37-46. doi: 10.1016/j.epsl.2018.05.032
- Reese, C. C., Solomatov, V. S. and Moresi, L. N. (1998) Heat transport efficiency for stagnant lid convection with dislocation viscosity: Application to Mars and Venus. *Journal of Geophysical Research: Planets*, **103**, 13643-13657. doi: 10.1029/98je01047
- Riner, M. A., Bina, C. R., Robinson, M. S. and Desch, S. J. (2008) Internal structure of Mercury: Implications of a molten core. *Journal of Geophysical Research: Planets*, **113**, E08013. doi: 10.1029/2007je002993
- Rivoldini, A., Van Hoolst, T., Verhoeven, O., Mocquet, A. and Dehant, V. (2011) Geodesy constraints on the interior structure and composition of Mars. *Icarus*, **213**, 451-472. doi: 10.1016/j.icarus.2011.03.024
- Rivoldini, A. and Van Hoolst, T. (2013) The interior structure of Mercury constrained by the low-degree gravity field and the rotation of Mercury. *Earth and Planetary Science Letters*, **377**, 62-72. doi: 10.1016/j.epsl.2013.07.021
- Robinson, M. S. and Taylor, G. J. (2001) Ferrous oxide in Mercury's crust and mantle. *Meteoritics & Planetary Science*, **36**, 841-847. doi: 10.1111/j.1945-5100.2001.tb01921.x
- Rückriemen, T., Breuer, D. and Spohn, T. (2015) The Fe snow regime in Ganymede's core: A deep-seated dynamo below a stable snow zone. *Journal of Geophysical Research: Planets*, **120**, 1095-1118. doi: 10.1002/2014je004781
- Rückriemen, T., Breuer, D. and Spohn, T. (2018) Top-down freezing in a Fe-FeS core and Ganymede's present day magnetic field. *Icarus*, **307**, 172-196. doi: 10.1016/j.icarus.2018.02.021
- Sanloup, C., Guyot, F., Gillet, P., Fiquet, G., Mezouar, M. and Martinez, I. (2000) Density measurements of liquid Fe-S alloys at high pressure. *Geophysical Research Letters*, 811-814. doi: 10.1029/1999GL008431
- Santo, A. G., Gold, R. E., McNutt, R. L., Solomon, S. C., Ercol, C. J., Farquhar, R. W., Hartka, T. J., Jenkins, J. E., McAdams, J. V., Mosher, L. E., Persons, D. F., Artis, D. A., Bokulic, R. S., Conde, R. F., Dakermanji, G., Goss, M. E., Haley, D. R., Heeres, K. J., Maurer, R. H., Moore, R. C., Rodberg, E. H., Stern, T. G., Wiley, S. R., Williams, B. G., Yen, C. W. L. and Peterson, M. R. (2001) The MESSENGER mission to Mercury: Spacecraft and mission

- design. *Planetary and Space Science*, **49**, 1481-1500. doi: 10.1016/S0032-0633(01)00087-3
- Schaefer, B. E. (2007) The latitude and epoch for the origin of the astronomical lure in MUL.APIN, in: *American Astronomical Society Meeting*, p. 157.
- Schubert, G., Cassen, P. and Young, R. E. (1979) Subsolidus convective cooling histories of terrestrial planets. *Icarus*, **38**, 192-211. doi: 10.1016/0019-1035(79)90178-7
- Schubert, G. and Spohn, T. (1990) Thermal history of Mars and the sulfur content of its core. *Journal of Geophysical Research: Solid Earth*, **95**, 14095-14104. doi: 10.1029/JB095iB09p14095
- Schubert, G. (2006) Thermal evolution of planets and satellites, in: *Encyclopedia of Planetary Sciences*, Shirley, J. H., Fairbridge, R. W. (Eds.). Springer Dordrecht, pp. 808-814.
- Solomon, S. C. (1976) Some aspects of core formation in Mercury. *Icarus*, **28**, 509-521. doi: 10.1016/0019-1035(76)90124-X
- Solomon, S. C., McNutt, R. L., Gold, R. E., Acuña, M. H., Baker, D. N., Boynton, W. V., Chapman, C. R., Cheng, A. F., Gloeckler, G., Head III, J. W., Krimigis, S. M., McClintock, W. E., Murchie, S. L., Peale, S. J., Phillips, R. J., Robinson, M. S., Slavin, J. A., Smith, D. E., Strom, R. G., Trombka, J. I. and Zuber, M. T. (2001) The MESSENGER mission to Mercury: Scientific objectives and implementation. *Planetary and Space Science*, 1445-1446
- Solomon, S. C. and Anderson, B. J. (2018) The MESSENGER mission: Science and implementation overview, in: *Mercury: The View After MESSENGER*, Solomon, S. C., Nittler, L. R., Anderson, B. J. (Eds.). Cambridge University Press, pp. 1-29.
- Sori, M. M. (2018) A thin, dense crust for Mercury. *Earth and Planetary Science Letters*, **489**, 92-99. doi: 10.1016/j.epsl.2018.02.033
- Spohn, T. and Schubert, G. (1982) Modes of mantle convection and the removal of heat from the Earth's interior. *Journal of Geophysical Research: Solid Earth*, **87**, 4682-4696
- Spohn, T. (1991) Mantle differentiation and thermal evolution of Mars, Mercury, and Venus. *Icarus*, **90**, 222-236. doi: 10.1016/0019-1035(91)90103-Z
- Stern, R. J., Gerya, T. and Tackley, P. J. (2018) Stagnant lid tectonics: Perspectives from silicate planets, dwarf planets, large moons, and large asteroids. *Geoscience Frontiers*, **9**, 103-119. doi: 10.1016/j.gsf.2017.06.004
- Stevenson, D. J., Spohn, T. and Schubert, G. (1983) Magnetism and thermal evolution of the terrestrial planets. *Icarus*, **54**, 466-489. doi: 10.1016/0019-1035(83)90241-5
- Strom, R. G. (1979) Mercury: A post-Mariner 10 assessment. *Space Science Reviews*, 3-70
- Takahashi, E. (1990) Speculations on the Archean mantle: Missing link between komatiite and depleted garnet peridotite. *Journal of Geophysical Research: Solid Earth*, **95**, 15941-15954. doi: 10.1029/JB095iB10p15941
- Tosi, N., Grott, M., Plesa, A. C. and Breuer, D. (2013) Thermochemical evolution of Mercury's interior. *Journal of Geophysical Research: Planets*, **118**, 2474-2487. doi: 10.1002/jgre.20168
- Tosi, N., Cadek, O., Behouňková, M., Kánová, M., Plesa, A. C., Grott, M., Breuer, D., Padovan, S. and Wiczorek, M. A. (2015) Mercury's low-degree geoid and topography controlled by insolation-driven elastic deformation. *Geophysical Research Letters*, **42**, 7327-7335. doi: 10.1002/2015gl065314
- Tosi, N. and Padovan, S. (2021) Mercury, Moon, Mars: Surface expressions of mantle convection and interior evolution of stagnant lid bodies, in: *Mantle Convection and Surface*

- Expressions*, Marquardt, H., Ballmer, M., Cottaar, S., Konter, J. (Eds.), Ch. 17, pp. 455-491.
- Turcotte, D. L. and Schubert, G. (2002) *Geodynamics*. Cambridge.
- Vander Kaaden, K. E. and McCubbin, F. M. (2015) Exotic crust formation on Mercury: Consequences of a shallow, FeO-poor mantle. *Journal of Geophysical Research: Planets*, **120**, 195-209. doi: 10.1002/2014JE004733
- Vander Kaaden, K. E. and McCubbin, F. M. (2016) The origin of boninites on Mercury: An experimental study of the northern volcanic plains lava. *Geochimica et Cosmochimica Acta*, 246-263
- Vander Kaaden, K. E., McCubbin, F. M., Nittler, L. R., Peplowski, P. N., Weider, S. Z., Frank, E. A. and McCoy, T. J. (2017) Geochemistry, mineralogy, and petrology of boninitic and komatiitic rocks on the mercurian surface: Insights into the mercurian mantle. *Icarus*, **285**, 155-168. doi: 10.1016/j.icarus.2016.11.041
- Vander Kaaden, K. E., McCubbin, F. M., Turner, A. A. and Ross, D. K. (2020) Constraints on the abundances of carbon and silicon in Mercury's core from experiments in the Fe-Si-C system. *Journal of Geophysical Research: Planets*, **125**, e2019JE006239. doi: 10.1029/2019JE006239
- Vilim, R., Stanley, S. and Hauck, S. A. (2010) Iron snow zones as a mechanism for generating Mercury's weak observed magnetic field. *Journal of Geophysical Research: Planets*, **115**, E11003. doi: 10.1029/2009je003528
- Watters, T. R. (2021) A case for limited global contraction of Mercury. *Communications Earth and Environment*, **2**, 9. doi: 10.1038/s43247-020-00076-5
- Weider, S. Z., Nittler, L. R., Starr, R. D., McCoy, T. J., Stockstill-Cahill, K. R., Byrne, P. K., Denevi, B. W., Head, J. W. and Solomon, S. C. (2012) Chemical heterogeneity on Mercury's surface revealed by the MESSENGER X-Ray Spectrometer. *Journal of Geophysical Research: Planets*, **117**, E00105. doi: 10.1029/2012je004153
- Weider, S. Z., Nittler, L. R., Starr, R. D., Crapster-Pregont, E. J., Peplowski, P. N., Denevi, B. W., Head, J. W., Byrne, P. K., Hauck, S. A., Ebel, D. S. and Solomon, S. C. (2015) Evidence for geochemical terranes on Mercury: Global mapping of major elements with MESSENGER's X-Ray Spectrometer. *Earth and Planetary Science Letters*, **416**, 109-120. doi: 10.1016/j.epsl.2015.01.023
- Wicht, J. and Heyner, D. (2014) Mercury's magnetic field in the MESSENGER Era, in: *Planetary Geodesy and Remote Sensing*, Jin, S. (Ed.). CRC Press, pp. 222-262.
- Williams, Q. (2009) Bottom-up versus top-down solidification of the cores of small solar system bodies: Constraints on paradoxical cores. *Earth and Planetary Science Letters*, **284**, 564-569. doi: 10.1016/j.epsl.2009.05.019

## Appendices

## A. Modified NORMS Calculation

MESSENGER XRS and GRS data were used to determine the mineralogical composition of the NSP (Anzures *et al.*, 2020; Namur *et al.*, 2016; Nittler *et al.*, 2018). The measured elemental ratios are Mg/Si, Al/Si, Ca/Si, Fe/Si, S/Si, Na/Si, and the concentrations of K, Ti, Mn, and Cr (from Nittler *et al.*, 2011; Peplowski *et al.*, 2012; Peplowski *et al.*, 2014; compiled by Vander Kaaden *et al.*, 2017; Weider *et al.*, 2015). Based on these compositions, and a silicon abundance estimate of 25 wt.% (Evans *et al.*, 2012; Vander Kaaden and McCubbin, 2016), stoichiometry was used to calculate the abundances of the following oxides: SiO<sub>2</sub>, TiO<sub>2</sub>, Al<sub>2</sub>O<sub>3</sub>, Cr<sub>2</sub>O<sub>3</sub>, FeO, MnO, MgO, CaO, Na<sub>2</sub>O, K<sub>2</sub>O, and the following sulfides: FeS, CrS, TiS<sub>2</sub>, MnS, MgS, and CaS. These oxide and sulfide abundances were used as inputs into a modified version of the CIPW norms following the methodology of Vander Kaaden and McCubbin (2016). The sulfur concentration recorded by MESSENGER was algorithmically redistributed into the sulfides following the trend of sulfide's affinity to bond with Fe, Cr, Ti, Mn, Mg, and Ca. Using a mass balance, the amounts of both the metal and sulfur content were removed from the initial conditions of the metal and sulfur. To determine how much sulfur was distributed into MgS and CaS, a partition coefficient ( $K_D$ ) of 1.97 was used (Vander Kaaden and McCubbin, 2016). A modification made to the CIPW norms calculation was to add the MnO to the FeO component before the major rock oxides were calculated. This prevented a calculation of the manganosite output, since the mercurian mantle was so reduced which would cause MnO to be consumed by olivine or pyroxene (Vander Kaaden *et al.*, 2017). After the sulfur was appropriately distributed within the sulfides, the CIPW normative calculation methodology described by Kelsey (1965) was utilized to determine the idealized surface mineral composition of the NSP (**Figure A-1**).

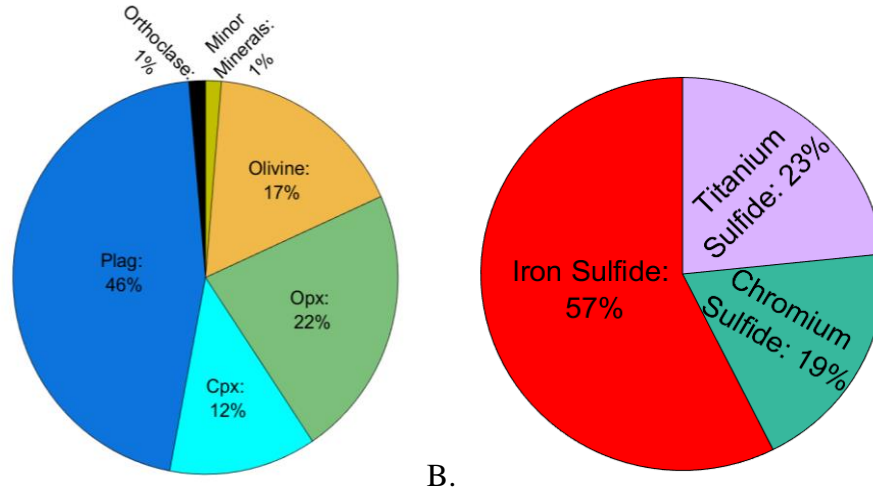


**Figure A-1:** (A) The major mineral breakdown of the non-sulfide bearing minerals of the NSP-HMg region. The main mineral components for this region were plagioclase, followed by orthopyroxene, olivine, clinopyroxene, orthoclase, and other minor minerals, described above. (B) The sulfide breakdown of the NSP-HMg region of the surface is shown here, which was found to be predominantly iron sulfide, then titanium sulfide, and chromium sulfide.

## B. Core Parameters

### B.1. The calculation of the inner and outer core density values

As stated in the text, the 3<sup>rd</sup> order Birch Murnaghan EoS was used to calculate the densities of the inner and outer core, with the thermodynamic parameters from *Komabayashi and Fei* (2010) for solid Fe, and *Sanloup et al.* (2000) and *Jing et al.* (2014) for liquid FeS parameters. The solid Fe density value was calculated over the pressure range of the solid inner core, if an inner core was formed. If an inner core was not formed, then the density of Fe was set to 0 kg/m<sup>3</sup>. The solid Fe density was plotted against the pressure range of the outer core to obtain a relationship between core pressure and the solid Fe density. As Mercury's core is thought to contain 2.8–8.9 wt.% S currently, this mass fraction was used to calculate the bulk modulus and the reference density for each FeS alloy: Fe-3 wt.% S, Fe-4 wt.% S, Fe-5 wt.% S, Fe-6 wt.% S, Fe-7 wt.% S, Fe-8 wt.% S, and Fe-9 wt.% S. The bulk modulus and reference densities were calculated using a quadratic form and are shown below:

$$K = K_a * \chi_S^2 + K_b * \chi_S + K_c \quad (\text{B-1})$$

$$\rho_0 = \rho_{0,a} * \chi_S^2 + \rho_{0,b} * \chi_S + \rho_c \quad (\text{B-2})$$

The coefficients for these equations are listed in Table B-1. Once these values were obtained, they were plugged into the EoS to determine the density profile throughout the entire core. An average of the density value was computed for each Fe+S composition, and then the averages were plotted as a function of S content (**Figure B-1**). As the light element concentration changed with each iteration of the model, the average density value of FeS was updated.

**Table B-1:** Liquid Fe+S Alloy Reference Bulk Modulus and Density Components

Parameter	Symbol	Value	Unit
Light Element Mass Fraction	X <sub>S</sub>	0.03-0.09	
Reference Bulk Modulus <sup>a</sup>	K <sub>a</sub>	780.8	GPa/X <sub>S</sub> <sup>2</sup>
Reference Bulk Modulus <sup>b</sup>	K <sub>b</sub>	-462.4	GPa/X <sub>S</sub>
Reference Bulk Modulus <sup>c</sup>	K <sub>c</sub>	85.9	GPa
Reference Density <sup>a</sup>	ρ <sub>0,a</sub>	31524	kg/m <sup>3</sup> /X <sub>S</sub> <sup>2</sup>
Reference Density <sup>b</sup>	ρ <sub>0,b</sub>	-20012	kg/m <sup>3</sup> /X <sub>S</sub>
Reference Density <sup>c</sup>	ρ <sub>0,c</sub>	7019	kg/m <sup>3</sup>

(*Jing et al.*, 2014; *Sanloup et al.*, 2000)

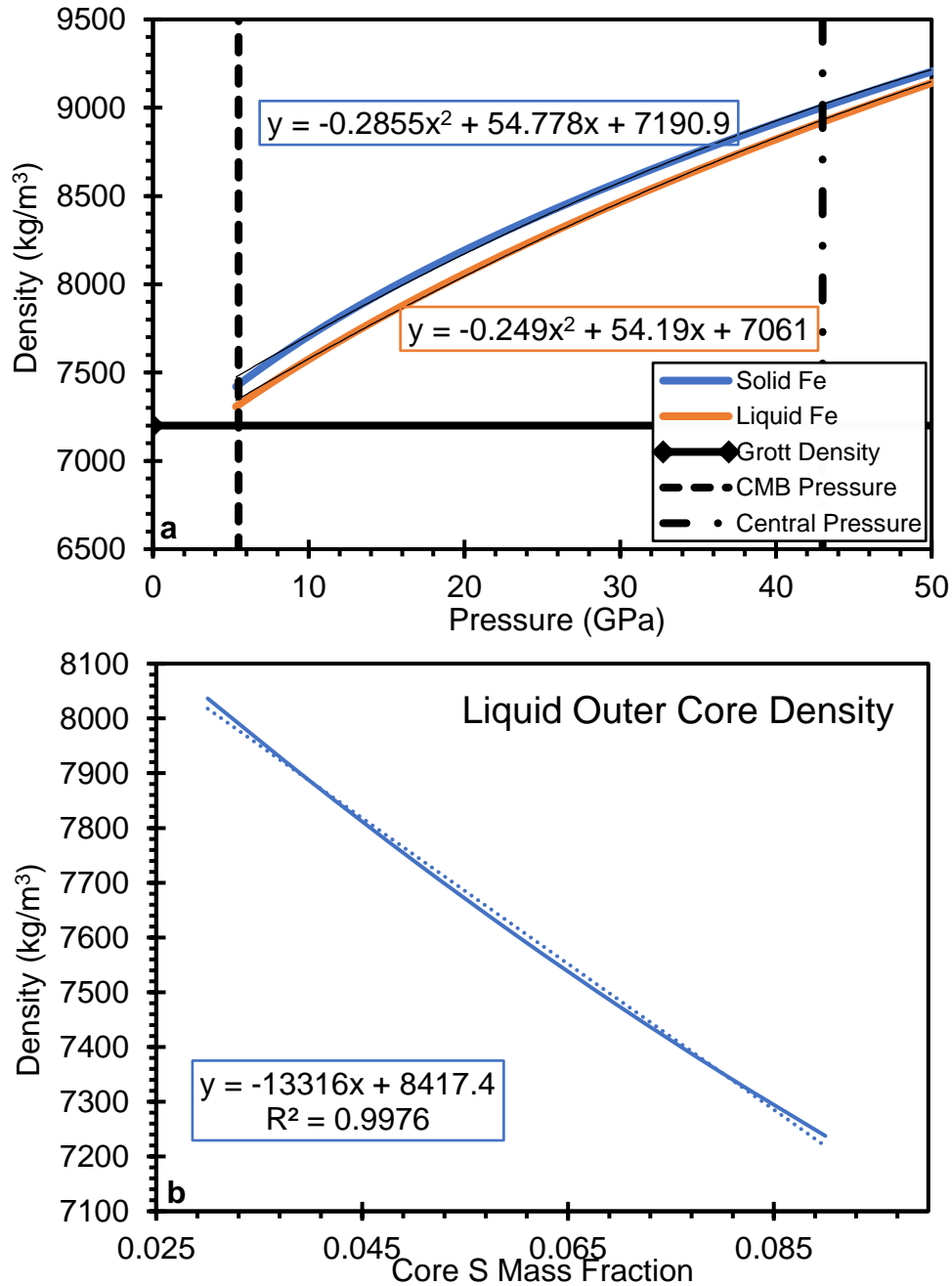


**Figure B-1:** (a) The solid and liquid Fe density relationship with the pressure of the core. The dark blue line shows the trend in the solid Fe density, while the brown line shows the trend in the liquid Fe density. The black dashed and dash-dot line indicate the pressure boundary of the CMB, and the central pressure of the planet, respectively. The black line indicates the constant core density used in the model created by *Grott et al.* (2011). (b) The liquid FeS density as a function of core S content.

## B.2. The Fe+S Melting Curve

Each term in the core adiabat and melt curve is calculated separately and then placed into the final equation to get the temperature of the melt curve, calculated over a pressure array:

$$T_{ad} = T_c \left( \frac{1+T_{a1}P+T_{a2}P^2}{1+T_{a1}P_m+T_{a2}P_m^2} \right) \quad (\text{B-3})$$

$$T_m(P, \chi_S) = T_{m,Fe} - \frac{T_{m,Fe}-T_e(P)}{x_e(P)} \chi_S \quad (\text{B-4})$$

where the coefficients  $T_{a1}$ ,  $T_{a2}$ ,  $T_{o,Fe}$ ,  $a_1$ ,  $a_2$ ,  $a_3$ ,  $T_{e,0}$ ,  $b_1$ ,  $P_{e,0}$ ,  $x_{e,\infty}$ ,  $c_1$ , and  $c_2$  are in **Error! Reference source not found.**,  $P$  represents the pressure array in Pa, and  $T_{m,Fe}$  is found by:

$$T_{m,Fe} = T_{o,Fe} + a_1P + a_2P^2 + a_3P^3 \quad (\text{B-5})$$

The eutectic temperature was calculated based on the linear fit performed by *Rivoldini et al.* (2011), as the eutectic temperature of FeS decreases or increases with pressure over specific pressure ranges, and reaches a minimum value at 14 GPa, and has an inflection point at 21 GPa as shown in their Figure 2a. This fit led to the equation below:

$$T_e(P) = T_{e,0} + b_1(P + P_{e,0}) \quad (\text{B-6})$$

The same logic was used to obtain the eutectic composition equation of FeS based on the same set of experimental data and is explained in *Rivoldini et al.* (2011). This eutectic composition decreases with increasing pressure as shown in their Figure 2b. The equation used is shown below:

$$x_e(P) = x_{e,\infty} + c_1e^{c_2P} \quad (\text{B-7})$$

A misprint occurred in the *Rivoldini et al.* (2011) paper, and so the model accounts for that by switching the  $a_1$  and  $a_2$  values for the melting temperature of solid Fe, removing the negative sign for the  $c_2$  exponent in in the eutectic composition equation, and adjusting the  $P_{e,0}$  coefficient for the pressures greater than 21 GPa based on a personal communication from Rivoldini in 2019.

To determine if an inner core is forming, the difference between the core adiabat and the core melt curve is taken. If the minimum value of this difference is greater than 0, the adiabat is always greater than the melt curve, so no inner core forms at all within Mercury. If the maximum value of this difference is less than 0, the adiabat is always less than the melt curve, so Mercury's core is fully solidified. However, if either of the above cases do not occur, an inner core is crystallizing within Mercury.

As the inner core can crystallize from the top-down or the bottom-up, both cases need to be considered here. Since the core adiabat and the core melt curve are calculated over pressure arrays from the center of the planet to the CMB, the intersection location between the two

temperature curves will indicate the method of inner core solidification. To determine where the intersection(s) occurs, the sign of the difference between the core adiabat and melt curve is observed and the location(s) where the sign switches from negative to positive and then positive to negative is where the intersection begins and ends. The negative value indicates the core is entering the intersecting region, while a positive value indicates the core is exiting the intersecting region. This sign change is based on the first value in the difference array which is set to either 0 or 1. If the first value is 0, a solid inner core is forming from the center outwards. If the first value is 1, the core has the potential for Fe snow crystallization. Depending on the location(s) of the intersection(s), one of two paths are followed, and are described in the main text.

**Table B-2:** Core Adiabat and Melt Curve Parameters

Parameter	Symbol	Value for all $P$			Units	Source
Core Adiabat Curve Coefficient	$T_{a1}$	8x10 <sup>-12</sup>			K/Pa	k
Core Adiabat Curve Coefficient	$T_{a2}$	-3.9x10 <sup>-23</sup>			K/Pa <sup>2</sup>	k
Core Melt Curve	$\alpha$	2.4				k
Sulfur Concentration Reference	$x_{e,\infty}$	0.11				l
Sulfur Curve Coefficient	$c_1$	0.187				l
Sulfur Curve Coefficient	$c_2$	-0.065			1/GPa	l
Iron Melting Reference Temperature	$T_{0,Fe}$	1811			K	l
Iron Melt Curve Coefficient	$a_1$	28.95			K/GPa	l
Iron Melt Curve Coefficient	$a_2$	-0.32			K/GPa <sup>2</sup>	l
Iron Melt Curve Coefficient	$a_3$	0.0013			K/GPa <sup>3</sup>	l
Parameter	Symbol	$3 \leq P < 14$ GPa	$14 \leq P < 21$ GPa	$21 \leq P < 60$ GPa	Units	Source
Eutectic Reference Pressure	$P_{e,0}$	3	14	21	GPa	l
Eutectic Reference Temperature	$T_{e,0}$	1268	1144	1346	K	l
Eutectic Temperature Coefficient	$b_1$	-11	29	13	K/GPa	l

k (Hauck et al., 2004), l (Rivoldini et al., 2011)

## C. Mantle Parameters

### C.1. Volumetric heat flux from radiogenic heating within the mantle

As the model starts with time  $(t) = 4.5$  Ga, the model time must be adjusted to calculate the radiogenic heat production in the mantle for the model. The time is adjusted by subtracting the current time of the model from 4.5 Ga to obtain the relevant time value for the calculation. Based on the XRS and GRS data from MESSENGER (*Nittler et al.*, 2018), it is clear that the mantle has to contain some amount of uranium ( $^{238}\text{U}$  and  $^{235}\text{U}$ ), thorium, and potassium (*Nittler et al.*, 2018). Using the mean mantle heat production rate equation from *Turcotte and Schubert* (2002), and the parameters in Table C-3, the amount of mantle radiogenic heating was calculated during each iteration of the run. However, as the planet evolves, the mantle forms partial melt which erupts to form crust. This enriches the crust in heat producing elements relative to the mantle. To determine the amount that is leaving the mantle, the model separates the total volumetric heating rate into the volumetric heating rate of the mantle and the volumetric heating rate of the crust. For this calculation, the masses of the crust ( $M_{cr}$ ) and entire mantle ( $M_m$ ; including both TBLs) is required.

$$M_{cr} = \frac{4}{3} \pi \left[ R_p^3 - (R_p - D_{cr})^3 \right] \rho_{cr} \quad (\text{C-1})$$

$$M_m = \frac{4}{3} \pi \left[ (R_p - D_{cr})^3 - R_c^3 \right] \rho_m \quad (\text{C-2})$$

The amount radiogenic heating in the mantle vs in the crust was calculated using a mass balance:

$$Q_{cr} = V \left( \frac{H}{\rho_m} \right) \rho_{cr} \quad (\text{C-3})$$

$$Q_m = H \left[ 1 + \frac{M_{cr}}{M_m} (1 - V) \right] \quad (\text{C-4})$$

where  $H$  represents the total radiogenic heat calculated for the time step. To ensure the model continues to run when the mantle is almost fully depleted of the radiogenic heat caused by decay of U, Th, and K (less than 10% of the total radiogenic heat in the simulation was in the mantle), a caveat was built into the algorithm to ensure model stability. This caveat sets the volumetric heat flux out of the mantle to be equal to 10% of equation (C-4) and set the volumetric heat flux out of the crust to be equal to 90% of equation (C-3), (*Grott*, 2022).

**Table C-3:** Heat producing element parameters

Parameter	Symbol	Value	Unit	Ref
<sup>238</sup> U Heat Release Rate	U <sup>238</sup> <sub>heat</sub>	9.46x10 <sup>-5</sup>	W/kg	g
<sup>235</sup> U Heat Release Rate	U <sup>235</sup> <sub>heat</sub>	5.96x10 <sup>-4</sup>	W/kg	g
Th Heat Release Rate	Th <sub>heat</sub>	2.46x10 <sup>-5</sup>	W/kg	g
K Heat Release Rate	K <sub>heat</sub>	2.97x10 <sup>-5</sup>	W/kg	g
log(2)/ <sup>238</sup> U Half Life	U <sup>238</sup> <sub>t</sub>	1.55x10 <sup>-10</sup>	1/yr	g
log(2)/ <sup>235</sup> U Half Life	U <sup>235</sup> <sub>t</sub>	9.845x19 <sup>-10</sup>	1/yr	g
log(2)/Th Half Life	Th <sub>t</sub>	4.98x10 <sup>-11</sup>	1/yr	g
log(2)/K Half Life	K <sub>t</sub>	5.546x10 <sup>-10</sup>	1/yr	g
<sup>238</sup> U Relative Abundance	U <sup>238</sup> <sub>abun</sub>	0.9928		g
<sup>235</sup> U Relative Abundance	U <sup>235</sup> <sub>abun</sub>	0.0071		g
Th Relative Abundance	Th <sub>abun</sub>	1		g
K Relative Abundance	K <sub>abun</sub>	1.19x10 <sup>-4</sup>		g

g (Turcotte and Schubert, 2002)

### C.1.1. Calculating the temperatures at the base of the stagnant lid and the bottom of the convecting mantle

The temperature at the base of the stagnant lid is calculated following equation 8 from *Morschhauser et al. (2011)* and follows principles described in (*Choblet and Sotin, 2000; Davaille and Jaupart, 1993; Grasset and Parmentier, 1998*). Mantle convection is driven by a temperature difference leading to a state of thermal convection. Following *Morschhauser et al. (2011)*, a Frank-Kamanetskii coefficient of 2.9 was used for Mercury to account for the spherical symmetry of the planet. With this term, the temperature at the base of the stagnant lid ( $T_{bsl}$ ) can be found using:

$$T_{bsl} = T_m - \theta(R/A)T_m^2 \quad (C-5)$$

where  $T_m$  is the mantle temperature input into the model,  $\theta$  is the Frank-Kamanetskii coefficient described above,  $R$  is the ideal gas constant, and  $A$  is the diffusion creep activation energy value.

In an analogous manner, the temperature at the bottom of the convecting mantle ( $T_{bcm}$ ) is calculated following equation 9 from *Morschhauser et al. (2011)*. Since the mantle is assumed to be adiabatic, this temperature can be found by calculating the adiabatic gradient and multiplying it by the region of the mantle that convects (the region between the top and bottom TBLs), and adding this product to the model's mantle temperature, with all the terms described in the main text.

$$T_{bcm} = T_m + \frac{\alpha_m g T_m}{c_m} (R_l - R_c - \delta_t - \delta_b) \quad (C-6)$$

### C.1.2. Calculating $\epsilon_m$ for the mantle

To calculate  $\epsilon_m$  for the mantle, a depth and radial profile were calculated for the mantle following the steps from *Grott (2022)*. The depth values were multiplied by the mantle's adiabatic gradient and then added to the mantle temperature to calculate an adiabatic mantle temperature profile. This adiabatic temperature profile was multiplied by the summed volume of the mantle using the integrated volumes calculated from the radial profile, and the temperature values were divided by the mantle to obtain the volumetrically averaged temperature value in the mantle. This average value is then divided by the mantle temperature in the model to calculate the ratio between the mantle temperature value and the average mantle temperature:

$$dT_m = \frac{\alpha_m g T_m}{c_m} \quad (C-7)$$

$$T_{m,adiab} = T_m + z_m dT_m \quad (C-8)$$

$$T_{m,eta} = \frac{1}{Vol_m} \int (4\pi r^2 T_{m,adiab} dr) \quad (C-9)$$

$$\epsilon_m = \frac{T_{m,eta}}{T_m} \quad (C-10)$$

### C.1.3. Calculating the thermal profile of the silicate part of Mercury

The thermal profile of the silicate part of Mercury was calculated in two steps as the cooling mechanism in the stagnant lid is conduction (*Morschhauser et al., 2011*), while the mantle can cool via convection or conduction. First the thermal profile through the stagnant lid ( $T_{lid,prof}$ ) was found by integrating the heat conduction equation from the base of the stagnant lid to the surface of the planet (*Grott, 2022*):

$$\frac{1}{r^2} \frac{\delta}{\delta r} \left( r^2 K_l \frac{\delta T}{\delta r} \right) + Q_l = 0 \quad (C-11)$$

where  $r$  is the radius of the planet,  $K_l$  and  $Q_l$  are the thermal conductivity and volumetric heat production rates of the regolith, the crust, and the mantle, respectively. Once integrated, this equation has the form:

$$T = -\frac{Q_l}{6K_l} r^2 - \frac{C_1}{K_l r} + \frac{C_2}{K_l} \quad (C-12)$$

where  $C_1$  and  $C_2$  are found with the following constraints. Due to the steady state of the model, the temperature and heat fluxes at each layer interface are consistent across the interface. The boundary conditions for the model are that the temperature at the surface of the planet is the surface temperature and the temperature at the base of the lid is the same value as calculated in equation (C-5). To calculate the change in the temperature profile with respect to radius, a finite difference

method was used. However, the thermal profile of the stagnant lid is flipped to ensure the thermal profile of the silicate outer portion of Mercury is calculated in the right direction (*Grott, 2022*). Following this, the surface heat flux is calculated by using the finite difference of the stagnant lid with respect to radius at the base of the lid and multiplying it by the thermal conductivity of the regolith.

Then, the thermal profile through the mantle was calculated. The mantle is split into three different sections for this calculation: the upper TBL, the convecting mantle, and the lower TBL. Since the convecting mantle is assumed to be adiabatic, the adiabatic gradient was added or subtracted (depending on the layer) to the temperature at the base of the stagnant lid, the mantle temperature of the model, and the CMB temperature of the model. The first temperature and radial profile was saved during each run. This final temperature profile is listed as  $T_{prof}$  in the main text.

#### *C.1.4. Calculating the thermal boundary layer thicknesses in the mantle*

The thermal boundary layer thicknesses are calculated using boundary layer theory from *Turcotte and Schubert (2002)*. The top thermal boundary layer is determined using the equation below, and all the terms are explained in the main text.

$$\delta_t = (R_l - R_c) * \left( \frac{Ra_{crit}}{Ra_m} \right)^\beta \quad (C-13)$$

The bottom thermal boundary layer thickness is calculated slightly differently due to strong dependence the mantle viscosity has on temperature, which makes the mantle more viscous at the base of the convecting mantle than at the top of the convecting mantle. Thus, the bottom thermal boundary layer thickness is calculated using the following equation and is set to the smaller thickness value of the two TBLs.

$$\delta_b = \min \left[ \delta_t, \left( \frac{\kappa f_p Ra_{i,crit} \eta_{TBL}}{\alpha_m \rho_m g_c |T_c - T_{bcm}|} \right)^\beta \right] \quad (C-14)$$

In the above equation,  $f_p$  is the pressure dependence of the viscosity on pressure (set to 1 as the viscosity is more strongly temperature dependent than pressure dependent),  $Ra_{i,crit}$  is the internal critical Rayleigh number,  $\eta_{TBL}$  is the calculated viscosity at the lower TBL for the average temperature within the bottom TBL, and  $g_c$  is the calculated gravity at the CMB. The internal critical Rayleigh number is given by the following set of equations:

$$Ra_i = \frac{g \rho_m \alpha_m (T_m - T_s + T_c - T_{bcm}) (R_p - R_c)^3}{\kappa \eta_m} \quad (C-15)$$

$$Ra_{i,crit} = 0.28 * Ra_i^{0.21} \quad (C-16)$$

The main difference between the mantle Rayleigh number, and the internal Rayleigh number is that the internal Rayleigh number accounts for all the fluid within the solid outer shell of Mercury, while the mantle Rayleigh number only accounts for the fluid within the convecting mantle. All the parameters used in this set of equations are described in the main text.

#### *C.1.5. Mantle convection velocity*

The final model calculation that needs to be discussed is the mantle convection velocity calculation. This calculation determines how fast the mantle mixes undepleted mantle material into the melt zone, which affects how much crust can grow in the model. As this is a measure of how fast the mantle is convecting, both the  $Ra_m$  and  $Ra_{crit}$  values are required here. The mantle convective velocity is calculated as:

$$u = u_0 \left( \frac{Ra_m}{Ra_{crit}} \right) \quad (C-17)$$

## D. Supplementary Data Visualizations: Relationships with Mantle Reference Viscosity and Initial Mantle Temperature

For all the following figures: Input mantle temperature increases from the left to the right, and the input sulfur content is shown by the color of the point, referenced to the color at the extreme right of the figure. Each x-value is plotted with a unique point marker, which is consistent with the plots discussed in Section 2.3. The first set are for varied mantle reference viscosity, the second set are for varied initial mantle temperature.

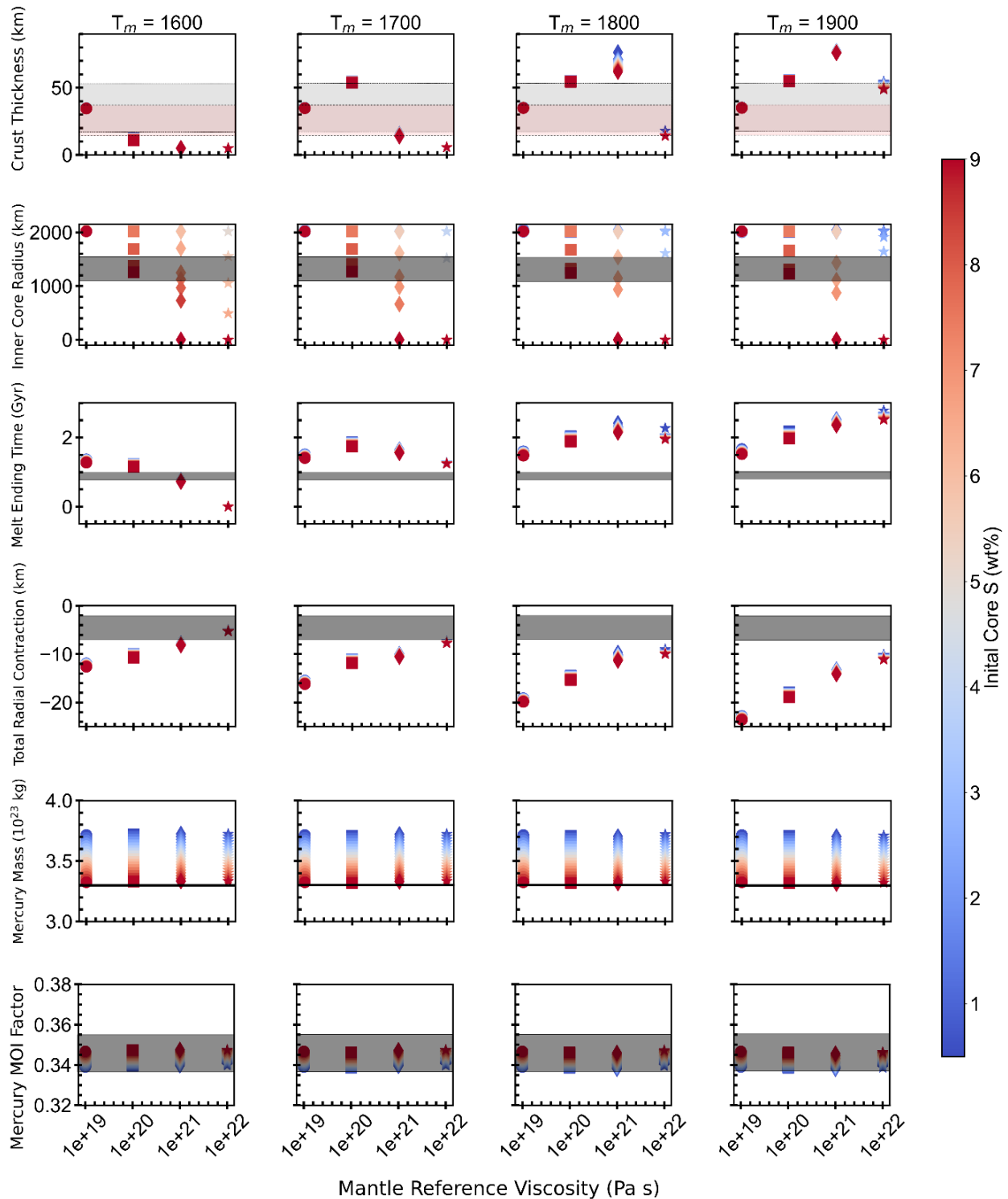


**Figure D-1:** Model result for varied mantle reference viscosity. **(First row)** The present day crustal thickness. The gray band indicates the bounds of the present day crustal thickness estimate: 15–53 km (*Padovan et al., 2015; Sori, 2018*), and models that have points plotted in the band represent models that have crustal thickness values which fit within the crust constraint. **(Second row)** The present day inner core radius. The gray band indicates the upper bound of the present day inner core estimate:  $1325 \pm 250$  km (*Breuer et al., 2015; Dumberry and Rivoldini, 2015*), and

models that have points plotted in or below the gray band represent models with appropriately sized present day inner core radii. **(Third row)** The timing of melt cessation. The gray band indicates the upper extent of melt generation (effusive volcanism) cessation by 3.7–3.5 Ga (*Byrne et al.*, 2016), and models that have points plotted in or below the gray band represent models with appropriate ending times for partial melt generation (effusive volcanism). **(Fourth row)** The present day total radial contraction. The gray band shows the bounds of the present day total radial contraction estimates: 2–7 km (*Byrne et al.*, 2014; *Claeys and Morbidelli*, 2015; *Watters*, 2021), and models with points plotted within the gray band represent models with appropriate total planet radial contraction values. **(Fifth row)** The present day Mercury mass. The black line shows the bounds of the present day Mercury mass and models with points plotted on the black line represent models with a present day mass that falls within the constraints. **(Sixth row)** The present day calculated Mercury polar MOI factor. The gray band shows the bounds of the present day Mercury polar MOI estimates, and models with points plotted within the gray band represent models with appropriate Mercury polar MOI factors.

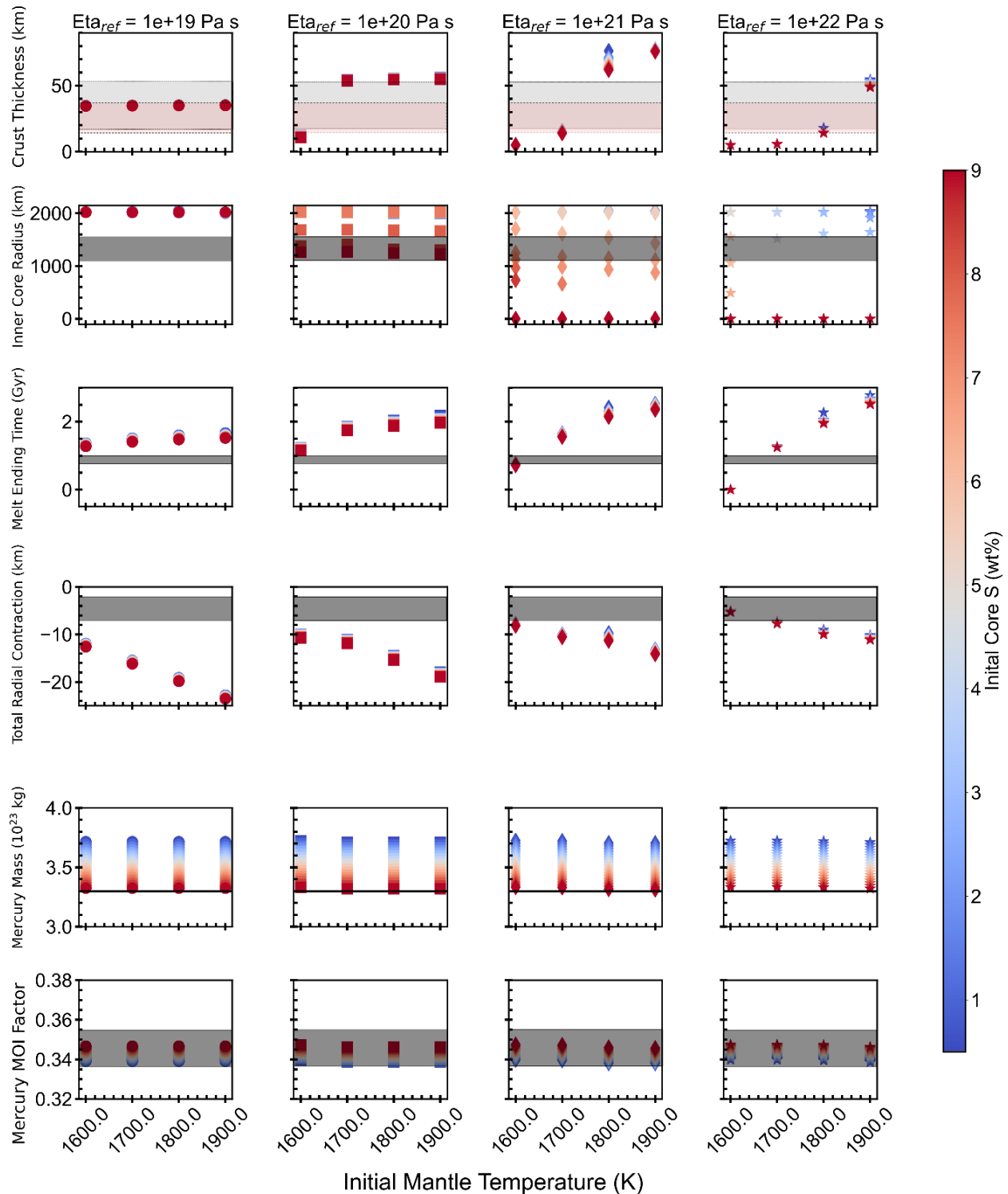


**Figure D-2:** Model result for varied initial mantle temperature. **(First row)** The present day crustal thickness. The gray band indicates the bounds of the present day crustal thickness estimate: 15–53 km (*Padovan et al., 2015; Sori, 2018*), and models that have points plotted in the band represent models that have crustal thickness values which fit within the crust constraint. **(Second row)** The present day inner core radius. The gray band indicates the upper bound of the present day inner core estimate: 1325  $\pm$  250 km (*Breuer et al., 2015; Dumberry and Rivoldini, 2015*), and models

that have points plotted in or below the gray band represent models with appropriately sized present day inner core radii. **(Third row)** The timing of melt cessation. The gray band indicates the upper extent of melt generation (effusive volcanism) cessation by 3.7–3.5 Ga (*Byrne et al.*, 2016), and models that have points plotted in or below the gray band represent models with appropriate ending times for partial melt generation (effusive volcanism). **(Fourth row)** The present day total radial contraction. The gray band shows the bounds of the present day total radial contraction estimates: 2–7 km (*Byrne et al.*, 2014; *Claeys and Morbidelli*, 2015; *Watters*, 2021), and models with points plotted within the gray band represent models with appropriate total planet radial contraction values. **(Fifth row)** The present day Mercury mass. The black line shows the bounds of the present day Mercury mass and models with points plotted on the black line represent models with a present day mass that falls within the constraints. **(Sixth row)** The present day calculated Mercury polar MOI factor. The gray band shows the bounds of the present day Mercury polar MOI estimates, and models with points plotted within the gray band represent models with appropriate Mercury polar MOI factors.

## E. Moment of Inertia Calculation

### E.1. Calculating planetary mass

The MOI and mass of Mercury was calculated in the model for each run. The mass was found by multiplying the density of each layer (i.e., the inner core, the outer core, the mantle, and the crust) by the integrated surface area of each layer. The radial bounds ( $R_{in}$ – $R_{out}$ ) for each layer are:  $0$ – $R_{ic}$  for the inner core,  $R_{ic}$ – $R_c$  for the outer core,  $R_c$ – $R_{cr}$  for the mantle, and  $R_{cr}$ – $R_p$  for the crust, following *Turcotte and Schubert* (2002):

$$M_{Mercury} = \rho_{layer} \int_{R_{in}}^{R_{out}} 4\pi R^2 \quad (E-1)$$

where  $M_{layer}$  is the mass of each layer,  $\rho_{layer}$  is the density of each layer, and  $R_{in}$  and  $R_{out}$  are replaced by the radial bounds in the text above. The total mass of Mercury was found by summing the masses of each layer together.

### E.2. Calculating moment of inertia factor

Once the total mass of Mercury was calculated, the MOI of each layer was possible to calculate. Using the basic MOI equation (*Turcotte and Schubert*, 2002), the MOI was calculated by:

$$I_{layer} = \frac{8}{3}\pi \int_{R_{in}}^{R_{out}} \rho_{layer} r^4 \quad (E-2)$$

where  $I_{layer}$  is the MOI of that layer. The total MOI of Mercury was calculated by summing MOIs of each layer together. To obtain the MOI factor (used as a constraint & described in 2.1.3), the total MOI was divided by the total mass.